18 A

PNL-2004-12
UC-90b,93

Development, Characterization and Evaluation of Materials for Open Cycle MHD

Quarterly Report
for the Period Ending September 1979

J. Lambert Bates
D. D. Marchant

November 1979

Prepared for the U.S. Department of Energy
under Contract DE-AC06-76RLO 1830

Pacific Northwest Laboratory
Operated for the U.S. Department of Energy
by Battelle Memorial Institute

PNL-2004-12

PACIFIC NORTHWEST LABORATORY
operated by
BATTELLE
for the
UNITED STATES DEPARTMENT OF ENERGY
Under Contract DE-AC06-76RLO 1830

Printed in the United States of America
Available from
National Technical Information Service
United States Department of Commerce
5285 Port Royal Road
Springfield, Virginia 22151

Price: Printed Copy $_____*; Microfiche $3.00

*Pages	NTIS Selling Price
001-025	$4.00
026-050	$4.50
051-075	$5.25
076-100	$6.00
101-125	$6.50
126-150	$7.25
151-175	$8.00
176-200	$9.00
201-225	$9.25
226-250	$9.50
251-275	$10.75
276-300	$11.00

PNL-2004-12
UC-90b,93

DEVELOPMENT, CHARACTERIZATION AND EVALUATION OF MATERIALS FOR OPEN CYCLE MHD

Quarterly Report for the Period Ending
September 1979

J. Lambert Bates
D. D. Marchant

November 1979

Prepared for the U.S. Department of Energy
under Contract DE-AC06-76RLO 1830

Pacific Northwest Laboratory
Richland, Washington 99352

TABLE OF CONTENTS

FIGURES

TABLES

1.0 SUMMARY

The development of hafnium-rare earth oxides, with demonstrated potential for MHD hot electrode, continues at a high level. Procedures for fabricating high density ceramic compacts with uniform microstructures at temperatures below 1875K for three compositions have been developed. Bars of these materials are being fabricated for testing in the Westinghouse WESTF facility. Yttrium chromites, which have also shown potential for hot electrodes, are being fabricated into test bars by a commercial supplier. These materials are being prepared for testing in WESTF. The required electrical conductivity and thermal conductivity have been, and are being, measured for these electrode materials.

The RFG air preheater refractory, tested in Montana State University's heat exchangers (Core #1) has been characterized and evaluated. The potential mechanism for corrosive attack by the molten slag have been identified.

2.0 OBJECTIVES AND SCOPE

The objectives of this program are to develop, test, characterize, and evaluate materials for open-cycle, coal-fired MHD power generators. The specific immediate goals emphasize electrode and insulator material, including: 1) testing and evaluation of the enhanced effects of alkali seed on materials in a dc electric field; 2) development and testing of improved electrodes and insulators with controlled microstructures, compositions, and properties; and 3) characterization and evaluation of materials relating to MHD power generator systems, including channel, combustor, and air preheater.

The scope of this program encompasses the following areas:

- Reproducible laboratory testing of both ceramic and metal electrode materials and insulator materials in alkali seed/slag under dc electric current and voltages as functions of temperature and seed/slag composition.
- Development and fabrication of electrodes, insulators, and other related materials with controlled electrical, chemical, and physical properties, including evaluation in laboratory tests in U.S. MHD test facilities.
- Characterization and evaluation of materials, including the measurement and analysis of structural, chemical, and thermophysical properties of electrodes, insulators, slag, and other related materials before and after testing.

3.0 TECHNICAL PROGRESS

3.1 MATERIALS DEVELOPMENT

The development of techniques for fabricating the hafnium-rare earth oxide electrode materials has continued.[1-3] Procedures for three compositions selected for further testing in MHD generators were established. Quality samples with high density, uniform microstructures were fabricated in quantity. Fabrication procedures for $YCrO_3$, previously developed, are now being used by a commercial company to produce a quantity of bars for future testing. The development of hafnium-rare earth oxide compositions and fabrication methods continues in conjunction with laboratory testing and evaluation.

3.1.1 Hafnium-Rare Earth Oxide Electrodes

Hafnium-rare earth oxides have demonstrated during laboratory tests excellent thermal stability, adequate electrical conductivity, and high electrochemical corrosion resistance in potassium seed and coal slags.[1-3] Further testing under simulated MHD conditions in the Westinghouse materials test facility (WESTF) is planned. However, bars with reproducible high density and similar microstructures are required. These materials, however, are not commercially available, and techniques for fabricating these compositions of interest as MHD electrodes have not been developed. It has been necessary, therefore, to develop such methods for powder and compact methods.

The development of fabrication methods has continued using coprecipitation methods. The fabrication procedures for four potential hafnium-rare earth oxide electrode materials were established. These compositions included:

$$0.29PrO_2 \cdot 0.05Yb_2O_3 \cdot 0.66HfO_2 \ ^*$$

$$0.06Tb_4O_7 \cdot 0.06Y_2O_3 \cdot 0.88HfO_2$$

*X-ray diffraction shows initial praseodymium oxide to be $PrO_{1.83}$. However, since oxygen content O_x mixed oxide is not known accurately, PrO_2 is used for convenience.

$0.10Er_2O_3 \cdot 0.10Tb_4O_7 \cdot 0.80HfO_2$

Bars of these were fabricated with uniform high density and microstructure for testing in a thermal MHD test at Westinghouse (WESTF 42) in coal slag and seed. Process capacity was increased to provide 100 to 300 grams per day depending upon composition. A sampling and archive system was established along with a coding system that identifies the composition, origin, and process step of each individual batch or portion of batch. This has permitted a quality evaluation of each specific sample which can be reviewed regarding further property and testing evaluation.

The typical process for fabricating these hafnium-rare earth oxides into quality, sintered compacts is outlined in the following flowsheet (Figure 1). The average properties of the powders and electrodes for the four principle compositions to be used in the WESTF-42 MHD materials test have been determined (Table 1). The various steps for fabrication are described in more detail.

3.1.1.1 Coprecipitation. The coprecipitation technique, a modification of that developed by Dole, et al.,[4] consists of the following steps: (1) The rare earth-oxide powders are dissolved in concentrated nitric acid and the hafnium oxychloride in water. (2) The solutions are diluted and mixed. (3) The mixed oxides are coprecipitated from the solution using ammonium hydroxide solution. (4) The precipitate is filtered and washed sequentially with water, acetone, toluene, and acetone then air dried. The resultant granular powder is a hydroxide salt that requires air calcination to form the oxide.

During coprecipitation acidic solution is dripped into rapidly stirred dilute ammonium hydroxide solution to insure proper mixing. A finer grain powder usually resulted when the solution is rapidly stirred. The amount of ammonium hydroxide is calculated to give an endpoint of precipitation at a pH of 8.5. A basic solution usually results in a powder that is easier to filter during the water washing.

The mixing of the powders and the wash medium is done with a Waring blender (3000-6000 ppm). The powder is filtered between washings using

FIGURE 1. Fabrication Hafnium-Rare Earth Oxides

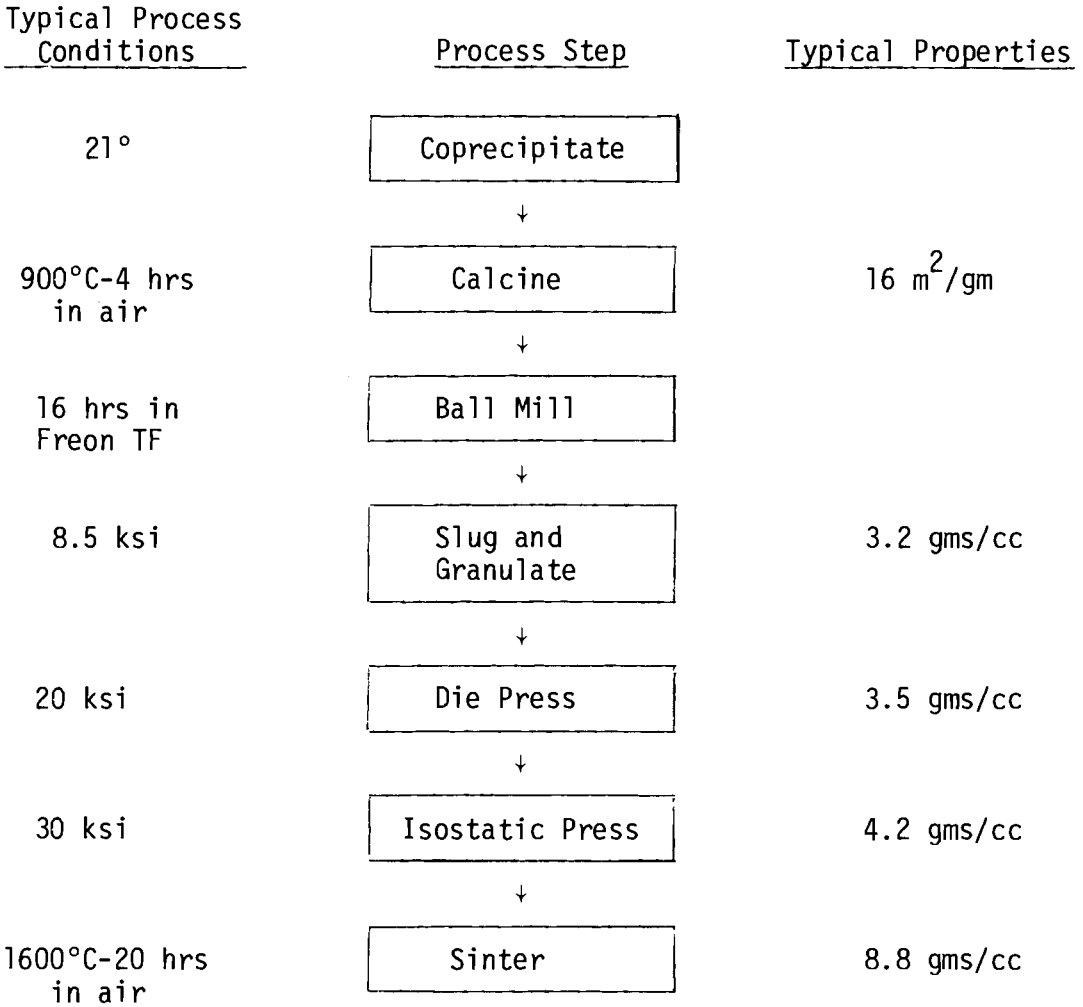

a Buchner filter with an ashless filter paper. The organic liquid washes are required to prepare a highly sinterable powder. Without these washes, the calcined powder does not have good flow characteristics or sintering behavior, even though the BET surface area remains high. The first acetone wash removes most of the bulk water. The toluene appears to remove the more tightly bound water and interacts with the unbonded surface sites. The last acetone wash removes the excess toluene and is a rapid drying medium. Several hours in a drying oven at 316K removes the acetone prior to calcining. The burning of acetone during air oxidation results in a powder with lower sinterability. (Burning of acetone will occur if the powder is not dried in a drying oven.)

3.1.1.2 Calcining. All calcining is done in air for four hours at a temperature between 1073 and 1273K. Calcining at lower temperatures did not remove sufficient volatiles resulting in weakening of the pressed compacts during sintering. Higher calcining temperatures resulted in powders with decreased sintering activity. The volume of the calcined powder is about two-thirds that of the uncalcined powder. X-ray diffraction analysis of the post calcined powder showed that for most of the compositions, the rare-earth stabilization of the hafnia powders occurred during calcining resulting in fluorite, pyrochlore, or monoclinic phases as predicted from phase equilibrium (Table 1).

3.1.1.3 Ball Milling. The powders were ball milled prior to pressing and sintering to break up the agglomerates that formed during calcination. The ball milling tended to increase the surface area. For example, the $0.29Pr_2O_3 \cdot 0.05Yb_2O_3 \cdot 0.66HfO_2$ powder for 0, 10, and 960 minutes had surface areas of 12.4, 14.4, and 16.1 m^2/g respectively. Ball milling also increased the flowability of the powders and the uniformity of the sintered material.

To minimize impurity contamination, Neoprene lined mills and ZrO_2 grinding balls were used in a Freon TF wet grinding media. The ZrO_2 resulted in less than 1 wt% ZrO_2 pickup in the final powder, and since

TABLE 1. Average Properties of Hafnium-Rare Earth Oxide Powders and Electrodes

Composition	Powder Surface Area*	X-Ray Density	Sintered Density	Phases**
A) 29 mole% PrO_2 5 " Yb_2O_3 66 " HfO_2	17 m^2/gm	9.0 gm/cc	98%	50% Cubic 50% Pyrochlore
B) 6 mole% Tb_2O_7 6 " Y_2O_3 88 " HfO_2	21 m^2/gm	9.6 gm/cc	93%	Fluorite
C) 10 mole% Er_2O_3 10 " Tb_4O_7 80 " HfO_2	16 m^2/gm	9.6 gm/cc	88%	Fluorite

* BET

** X-ray diffraction

it has properties nearly identical to HfO_2, its contamination should influence the final product less than other oxide contaminants.

Freon TF vaporized easily and was a better media than acetone, toluene, or ethyl, methyl, or isopropyl alcohol. Although ball milling resulted in lower green densities of the cold pressed oxide, the final sintered densities were higher.

3.1.1.4 Slugging and Granulation. The powders are slugged at 69 MPa (10,000 psi) before passing through a -14 mesh Tyler screen. The final sintered density is increased by about 5% (94% instead of 89%) by slugging and granulation of the powder.

3.1.1.5 Pressing. The slugged and granulated powder is pressed uniaxially in steel dies (with a 0.01 cm/cm topic) at 152 MPa (22,000 psi) into right parallelpipeds. The die and punch are lubricated with zinc stearate or lithium stearate. Humidity from the air is an adequate binder.

Isostatic pressing is used for final compaction after uniaxial pressing. This provides a more uniform application of pressure reducing some residual stresses resulting in a crack free compact with a uniform microstructure. The green pellets are isostatically pressed in double rubber (plastic) evacuated containers in a water soluble oil at 228 MPa (33,000 psi).

3.1.1.6 Sintering. The hafnium-rare earth oxide pellets are sintered between 1850 - 1875K in air. Sintering times are 16 hours with 5 hour heatup and cooldown cycle.

Sintering has also been studied in vacuum to 2275K in tungsten heating elements. Pellets to 98% of the theoretical density can be fabricated. Although no rare-earth oxide loss occurs, the oxide darkens because of reduction due to low oxygen pressure in the furnace. Reoxidation is performed at 1875K in air for 5 hours.

Some effects of the fabrication variables on the green density of the hafnium-rare earth oxides is summarized in Figure 2.

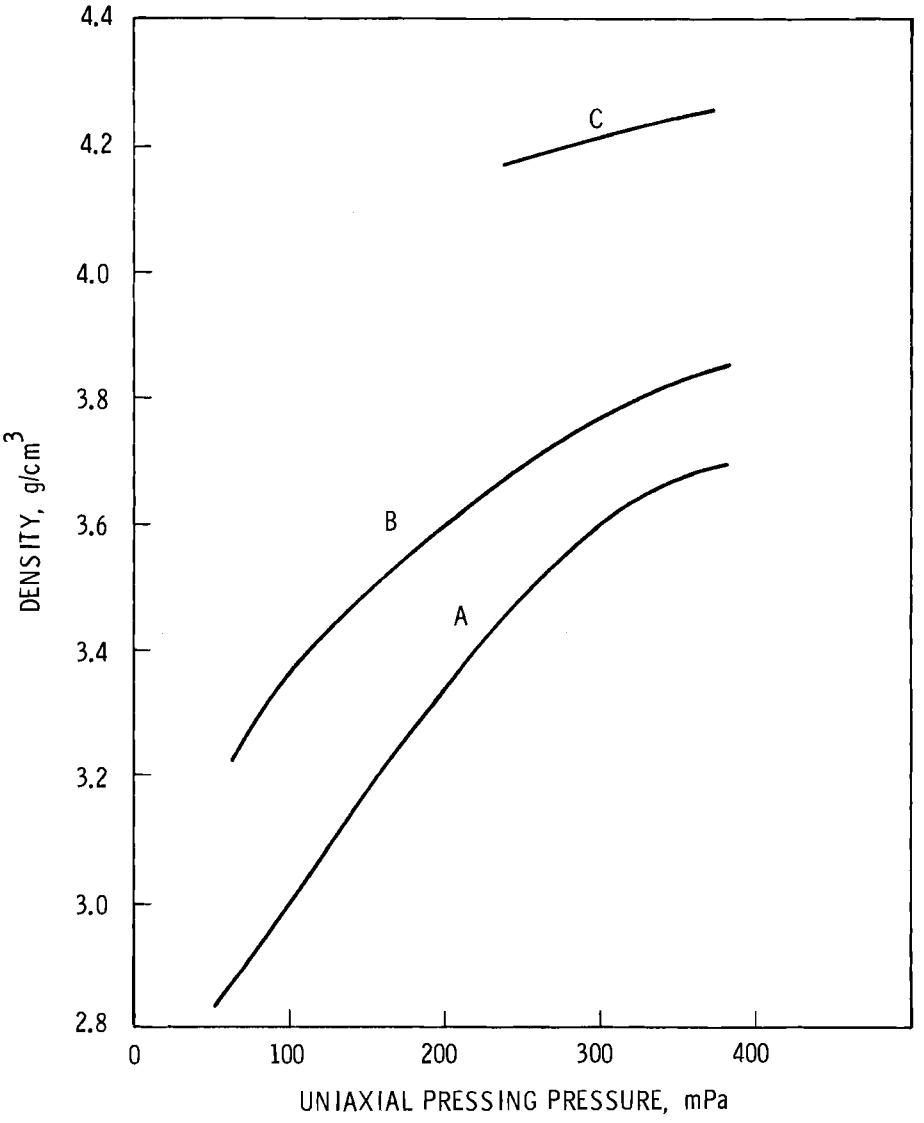

FIGURE 2. Green Density as a Function of Pressing Pressure of Powder CCC $Er_{0.14}Tb_{0.29}Hf_{0.57}O_2$.
A. Uniaxially pressed only.
B. Uniaxially pressed and isostatically pressed at 218MPa.
C. Ball milled powder, uniaxially pressed and isostatically pressed at 218 MPa.

3.1.2 Yttrium Chromite

Yttrium chromite is being fabricated by a commercial supplier on specifications provided by this laboratory. The $YMg_{0.05}Cr_{0.95}Cr_{0.95}O_3$ will be fabricated into bars for future testing under MHD conditions. The chromite will be characterized and properties measured electrochemically for tests in the laboratory and in an MHD generator (WESTF).

3.2 CHARACTERIZATION AND EVALUATION

A number of materials or material systems are being characterized and evaluated in support of other U.S. MHD programs relating to open cycle, coal fired MHD. These materials are received from other DOE MHD facilities, and are characterized using Pacific Northwest Laboratory facilities to provide information to assist in the technical progress of their programs. Now being characterized for evaluation are:

- Platinum coated copper anodes from AVCO test in Mark VII using coal slag and K_2SO_4 seed.
- Air preheater refractories (RFG) and slag tested at Montana State University's heat exchanger, Core No. 1.
- Potential air preheater refractories with varied compositions and structures tested in Montana State University's heat exchanger.
- Coal slags deposited on the Pt-Cu electrodes during a slagging seed experiment in Stanford University's MHD test facility.

The characterization and evaluation of the RFG refractory from MSU's heat exchanger has been completed, and the study of the others is continuing. The major work on AVCO's platinum coated copper anode is completed, and results will be reported next quarter.

3.2.1 Characterization of RFG Refractory Tested in MSU Heat Exchanger, Core No. 1

Selected cores of sinter bonded RFG refractory* tested in Montana State University's heat exchanger (Core #1) were examined to determine

*Corhart Refractories

the performance using a potassium seed free Montana "rosebud" type slag. Examination included optical ceramography and quantitative SEM-EDX characterization. Sections were taken from various bricks in the core which had operated at different temperatures. The heat exchanger core included six runs using four different slags with the major portion of the test, Runs 1, 2, and 6 of 50, 100, and 750 hours respectively, using the same slag. Runs 3, 4, and 15 (100 hours each) used different slags. All slags were similar in composition and can best be represented by comparing slag #6 with an average for all slags (Table 2).

The RFG used in the core was sintered bonded with a nominal composition shown in Table 3. The reported density was $\sim$3.26 g/cm^3 with $\sim$14% porosity. The porosity was generally open. The original structure was multiphase (Figure 3) with a primary MgO phase ($\sim$96% purity),[†] a lighter spinel phase (up to $\sim$0.03 mm) with a composition near 0.6 MgO$\cdot$ 0.4[$(Cr,Al,Fe)_2O_3$] with the Cr/Al/Fe ratios of 4/5/1, and small MgO rich spinel second phase, ($\sim$0.01 mm) near 0.75MgO$\cdot$0.25 [$(Cr,Al,Fe)_2O_3$] with a similar Cr/Al/Fe ratio. A very much smaller dendrite-like phase, (0.001 - 0.003 mm) even higher in MgO ($\sim$83%) [Al $\simeq$ Cr $\simeq$ Fe] and higher in Fe_2O_3 was also observed.

Each section was cut, mounted in resin, polished for metallographic examination and subsequent SEM and quantitative EDX evaluation. The general characterization and evaluation results are summarized in Table 4. The calculated minimum and maximum temperatures during the test, as reported by MSU, are also listed. The attack of the slag on the RFG was similar for all cores examined. The lowest temperature core, (1077 - 1094K) 49-2 (HM-5) remained essentially unchanged. In the other cores, the slag had penetrated the open pores and coated the exposed surfaces to various thicknesses and had reacted with the RFG, especially on the surfaces, altering the MgO-spinel structure. The reactions were greatest at the highest temperature core (1668 - 1723K) 2-2 (HM-1) where none of the original residual structure remained and least at the lower temperatures 49-2 (HM-4) (1412 - 1442K) where substantial residual RFG structure remained. The slag coating thickness was greatest on the 5-2 (HM-2) (1630 - 1638K) where some holes were completely closed.

[†]The phase notation used in the microstructures are defined in Table 5.

TABLE 2. Slag Compositions

	Analysis #6	Overall Runs
P_2O_3	0.75	0.65
SiO_2	53.5	53.25
MgO	9.14	9.85
Na_2O	0.51	0.40
K_2O	0.18	0.19
Al_2O_3	17.3	18.53
CaO	18.66	14.54
Fe_2O_3	4.06	3.68

*Taken from near top of bed.

TABLE 3. RFG (Nominal Compositions)

	As Reported	SEM-EDX
MgO	55-56%	63
Cr_2O_3	20%	16
Al_2O_3	8.0	6
FeO	11.0	11
SiO_2	2.5	3
CaO	0.5	1
TiO_2	1.5	1

Density: 3.26 g/cm^3

Porosity: 14%

Thermal Expansion Coefficient: 10.8×10^{-6}

TABLE 4. Microstructure of RFG After Testing

Sample Max.-Min. Temperature	General Appearance	Slag/RFG Interface: Slag Thickness on Surface(mm)	Slag/RFG Interface: Silicate Phase(s)	Slag/RFG Interface: Crystalline Phase(s)	RFG/Slag Interior: Silicate Phase(s)	RFG/Slag Interior: Crystalline Phase(s)
0-0 (HM-6) reference as fabricated	Dark brown black	-	-	-	-	Matrix MgO(95%)+0.03 mm size $0.6MgO \cdot 04(Cr_{0.4}Al_{0.5}Fe_{0.1})_2O_3$ (spinel s.s.) plus <0.005 mm spinel phases higher in Mg and Fe
49-2 (HM-5) (1077-1094K)	Very dark brown with light powder deposit on hole surfaces (smearable)	0	-	-		Same as original RFG HM-6
23-2 (HM-4) (1412-1442K)	Med. dark brown with slag coating some holes with light dark color	0 - 1 mm	$MgO \cdot 2CaO \cdot 2SiO_2$+Al adjacent to crystalline phases; slag composition altered	$2MgO \cdot SiO_2$; $Mg(Al,Cr,Fe)_2O_4$ high in Mg with Al/Cr/Fe ≈ 4/1/1	$MgO \cdot 2CaO \cdot 2SiO_2$; slag penetrated entire sample; depleted in Mg	$Mg(Al,Cr,Fe)_2O_4$ high in Mg with variable Al/Cr/Fe from 4/1/1 to 1/1/1; MgO
14-2 (HM-3) (1517-1562K)	Med. dark brown coated with dark slag; pores filled	1 mm	Phase separated $MgO \cdot 2CaO \cdot 2SiO_2$ (+4% Al_8O_3) + vitreous phase lower in Ca	$2MgO \cdot SiO_2$(+Ca); minor $Al_2O_3 \cdot 2SiO_2$ +20%(Ba,Ca)	$MgO \cdot 2CaO \cdot 2SiO_2$ with slag penetration entire sample	MgO; some islands RFG remaining but altered; Mg depleted (~15%) $Mg(Al,Cr,Fe)_2O_4$
5-2 (HM-2) (1630-1683K)	Med. brown color; all surfaces covered with brown slag; some holes closed	>5 mm	$MgO \cdot 2CaO \cdot 2SiO_2$ with some Al and iron	$2MgO \cdot SiO_2$; $Mg(Al,Cr,Fe)_2O_4$ with Al/Cr/Fex 4/1/1	$MgO \cdot 2CaO \cdot 2SiO_2$	$2MgO \cdot SiO_2$; $Mg(Al,Cr,Fe)_2O_4$ with variable Al/Cr/Fe ratio 4 to 1; little RFG remains
2-2 (HM-1) (1668-1723K)	Dark brown, holes enlarged, surface rough, no slag on surface	0 to<0.01 mm	-	-	$CaO \cdot Al_2O_3 \cdot 2SiO_2$ with stringers	Stringers of $2MgO \cdot SiO_2$; particles of $Mg(Al,Cr,Fe)_2O_4$ with Al/Fe~1/3, little Cr

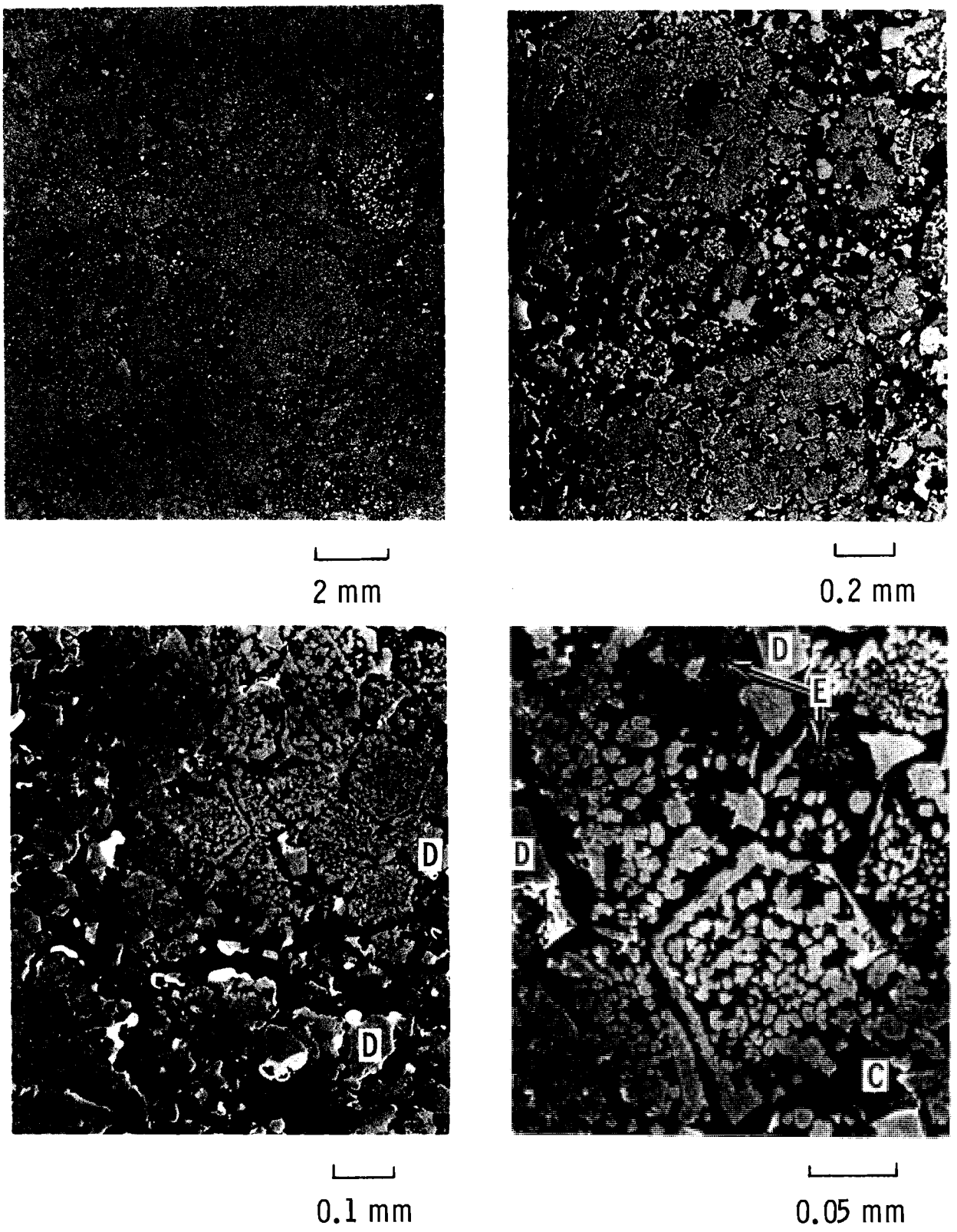

FIGURE 3. Microstructure of as fabricated RFG refractory before testing. See Table 5 for notation of phases.

TABLE 5. Microstructure Labels for Figures

A	Original RFG
B	Slag (altered)
C	MgO (periclase) (mp-3100K)
D	$0.6MgO \cdot 0.4(Al,Cr,Fe)_2O_3$ with Al/Cr/Fe ratio 4/1/1 (spinel s.s.) (mp $\sim$ 2200-2500K)
E	$0.75MgO \cdot 0.25(Al,Cr,Fe)_2O_3$ (spinel s.s.) (mp $\sim$ 2200-2500K)
F	$Mg(Al,Cr,Fe)_2O_4$ with Al/Cr/Fe - 4/1/1 (spinel s.s.)
G	$Mg(Al,Cr,Fe)_2O_4$ with Al/Cr/Fe $\simeq$ 1 (spinel s.s.)
H	$2MgO \cdot SiO_2$ (forsterite) (mp 2163K)
I	$MgO \cdot 2CaO \cdot 2SiO_2$ (akermanite) (mp 1723K)
K	$CaO \cdot Al_2O_3 \cdot 2SiO_2$ (anorthite) (mp 1826K)
L	$Mg(Al,Fe)_2O_4$ with Al/Fe = 1/3 (spinel s.s.)

mp - melting point

3.2.1.1 23-2 (HM-4) 1412 to 1442K. The lowest temperature RFG where reactions with slag were observed best defines the reactions which occurred between the RFG and the slag. The EDX mapping of the surface indicates that the SiO_2 had reacted with the MgO in the RFG at the exposed surfaces forming $2MgO \cdot SiO_2$ [forsterite, MP 1890°C] with the CaO remaining with the silicate slag (Figures 4, 5, and 6). The $Mg(Al,Cr,Fe)_2O_4$ phase in the RFG did not appear to react since the Al,Cr, and Fe remained combined at the surface and free of Si and Ca. However, the Al from the slag may have reacted with the spinel phase, as evidenced by the increased Al concentration at the surface.

The phases surrounding the $2MgO \cdot SiO_2$ particles (Figure 5) consisted of a near $MgO \cdot 2CaO \cdot 2SiO_2$ phase and $Mg(Al,Cr)_2O_4$ spinel (with Al/Cr from 4 to 1), Figure 4.

In the interior, the changes are less severe, with the residual RFG structure remaining, Figure 6. These residual particles are surrounded by Mg rich $Mg(Al,Cr)_2O_4$ and MgO phases. These are subsequently surrounded by $2MgO \cdot SiO_2$ particles and Mg rich $MgO \cdot 2CaO \cdot 2SiO_2$ similar to that at the surface.

3.2.1.2 14-2 (HM-3) 1517 to 1562K. The slag penetrated the entire sample with a slag-core interface very similar to the lower temperature 23-2 (HM-4). Crystalline particles of $2MgO \cdot SiO_2$ [+ 2.3 mol% CaO] were found in the altered slag at the RFG-slag interface (Figures 7 and 8). The altered slag contained three phases which may be crystalline. There were equal amounts of $MgO \cdot 2CaO \cdot 2SiO_2$ (with some few percent Al_2O_3), MgO (18 at.%) containing slag without chromium and unknown crystalline particles possibly $Al_2O_3 \cdot 2SiO_2$, with substantial amounts of Ca (10 at.%) and Ba (11 at.%).

The x-ray maps of the interface indicate that chromium and iron tend to remain with the aluminum after the MgO has reacted with the SiO_2. The calcium does not appear to be involved in the reaction since it concentrates in the altered slag which contains only small amounts of MgO.

The interior contained reaction products of $2MgO \cdot SiO_2$ and particles of Mg rich $Mg(Cr,Al)_2O_4$ spinel with $Cr \simeq Al$ and $Mg(Cr_{0.2}Al_{0.8})_2O_4$ also rich in Mg (Figure 8). These latter solid solutions exhibited variations between these two compositions. Some residual structure remained as islands in these reaction products.

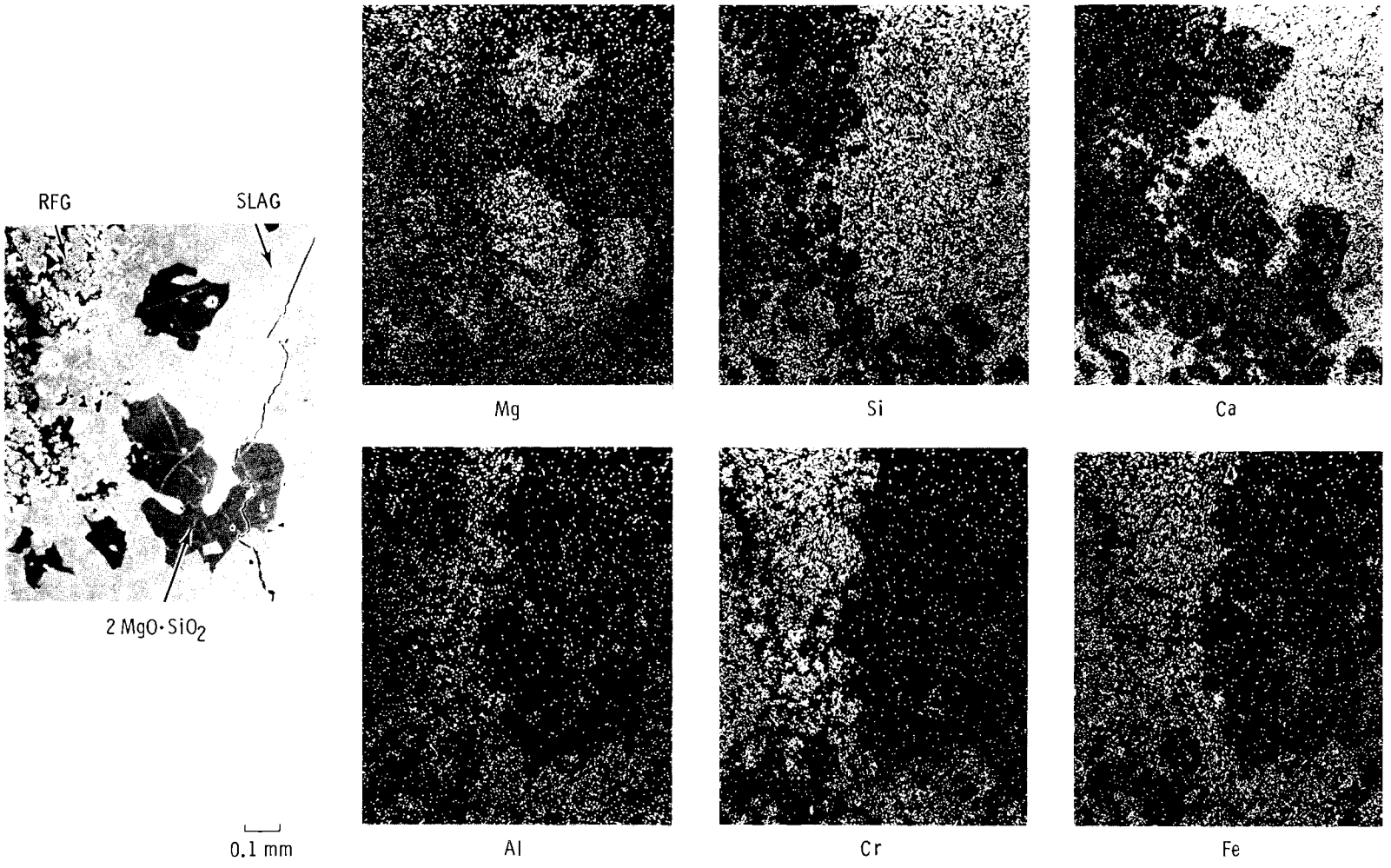

FIGURE 4. X-ray EDX mapping of RFG-slag interface for 23-2 (HM-4) tested at 1412-1442K.

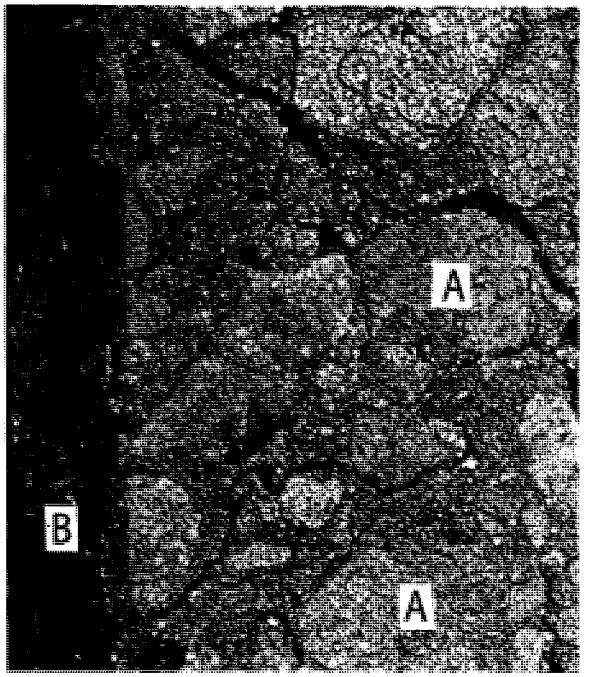

2 mm

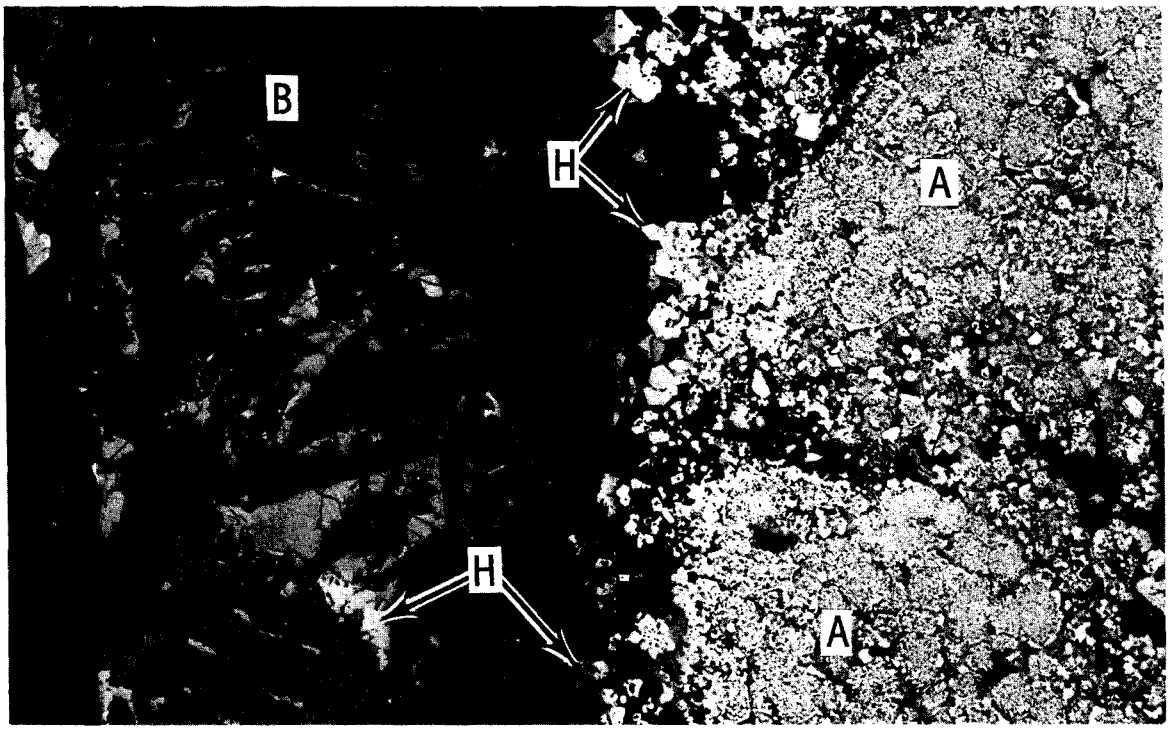

0.2 mm

FIGURE 5. Microstructure of RFG 23-2 (HM-4) Tested at 1412-1442K. See Table 6 for notations.

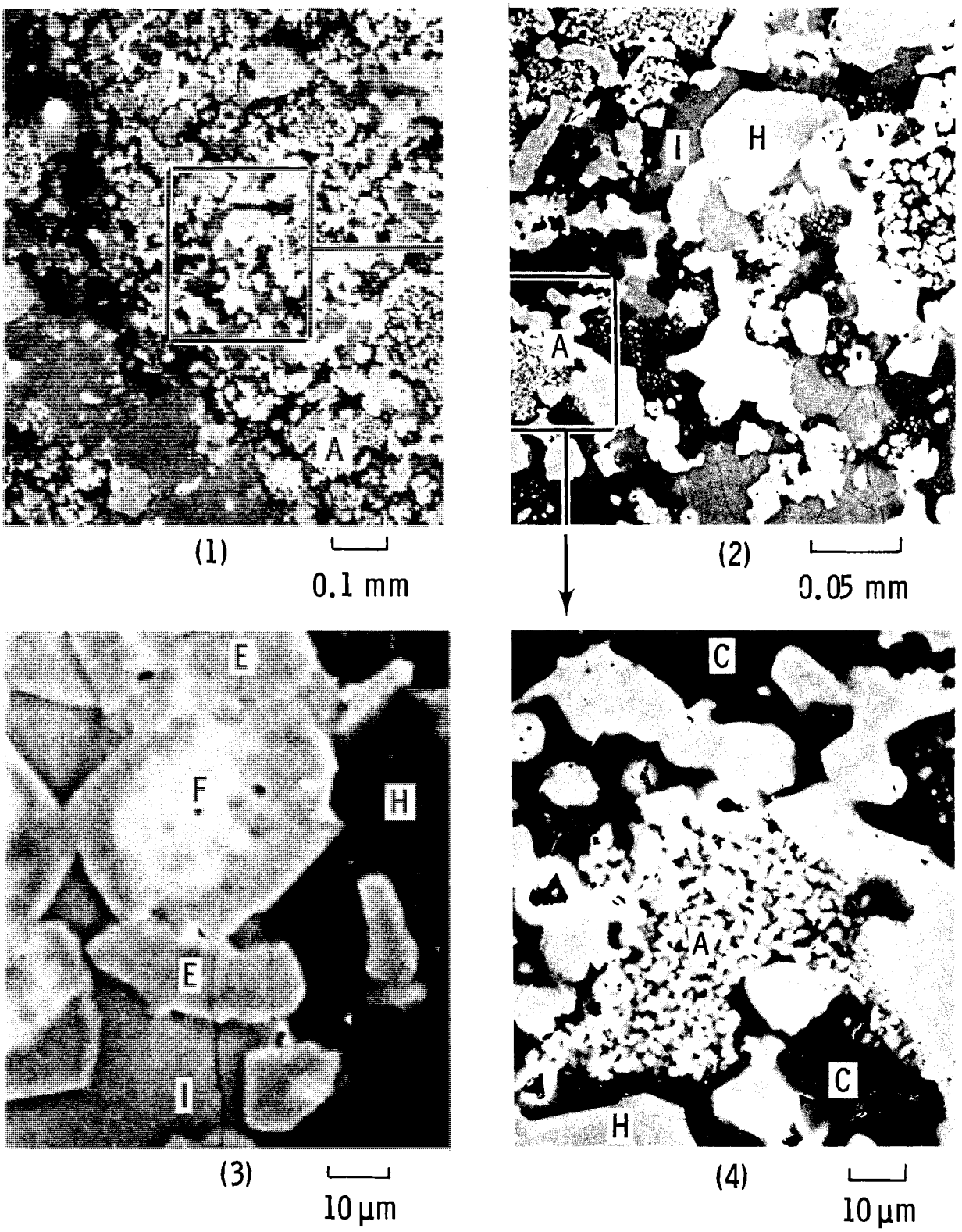

FIGURE 6. SEM microstructure of RFG 23-2 (HM-4) tested at 1412-1442K. 1, 2, and 3 are interior structures and 4 is slag-RFG interface. See Table 5 for notations.

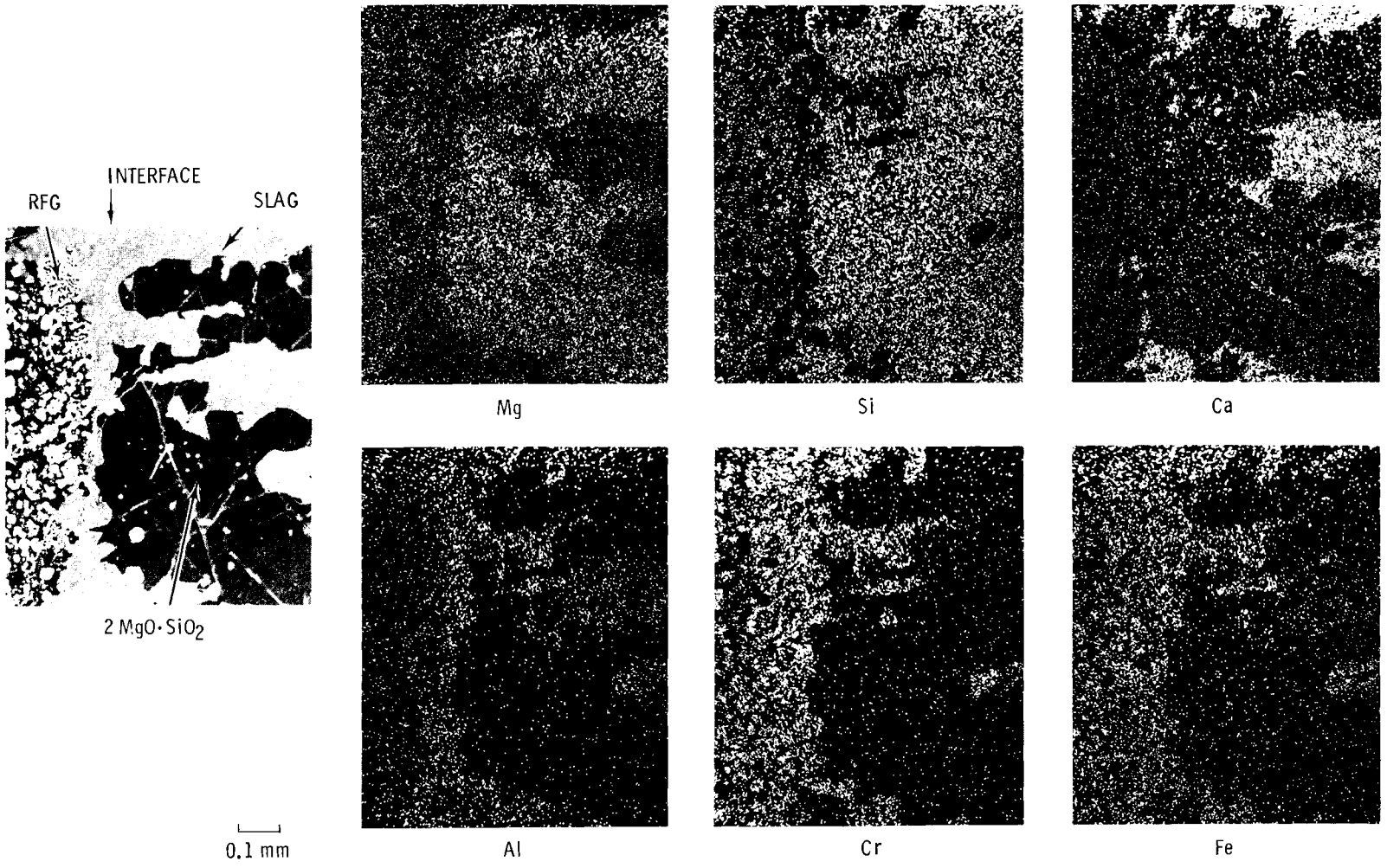

FIGURE 7. EDX x-ray mapping of RFG 14-2 (HM-3) tested at 1517-1562K. See Table 5 for notations.

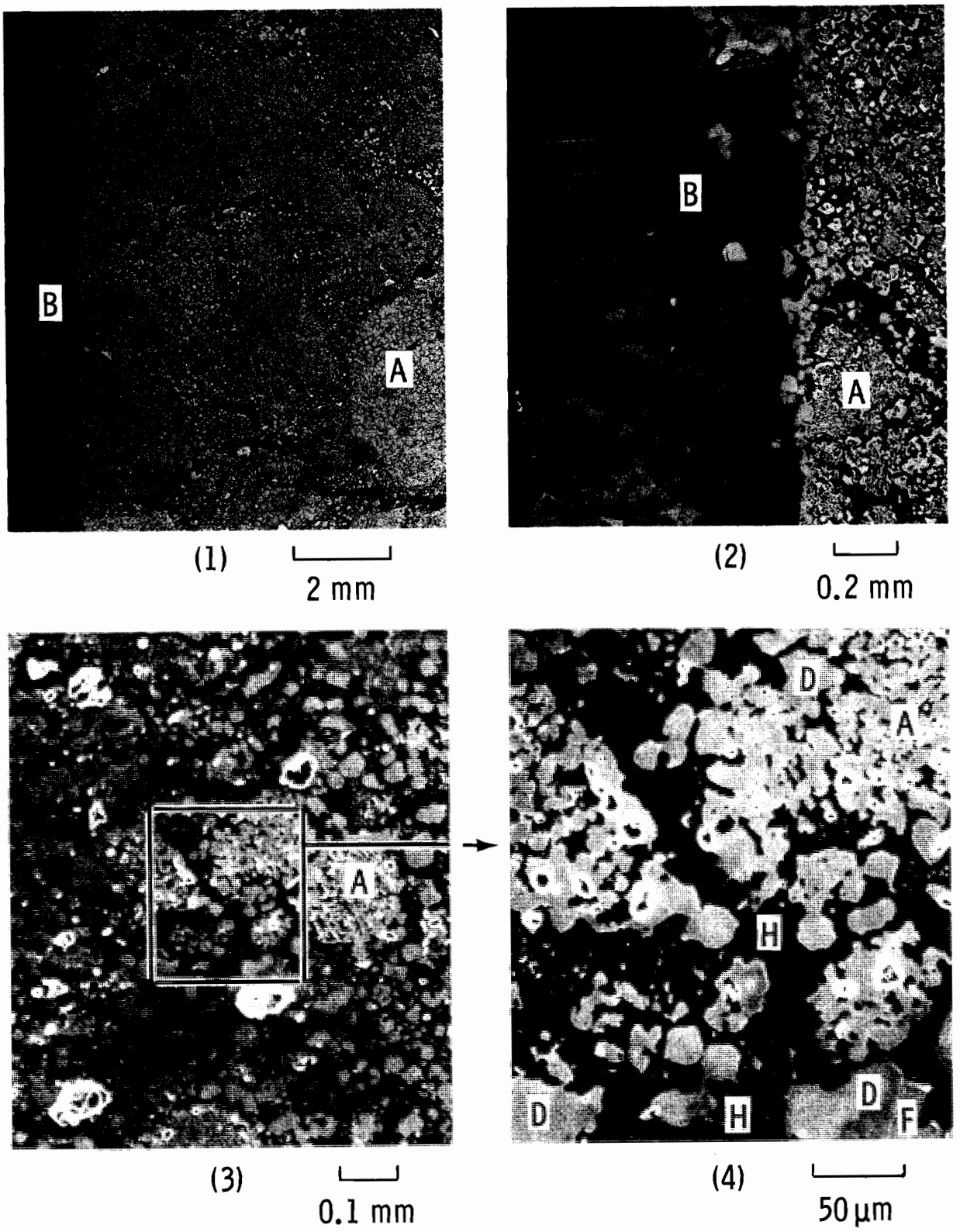

FIGURE 8. Microstructure of RFG 14-2 (HM-3) tested at 1517-1562K. See Table 5 for notations.

3.2.1.3 5-2 (HM-2) 1630 - 1683K. The slag layer in the core passages was substantially greater and had penetrated and reacted with the core material leaving only a few islands of the original structure (Figure 9). The interface particles of 2 $MgO \cdot SiO_2$ occurred in a higher concentration than in those bricks operating at lower temperatures. The slag surrounding these particles was again enriched in Ca and depleted in Si. At the immediate slag-RFG interface, $Mg(Al,Cr,Fe)_2O_4$ (Al/Cr/Fe 4/1/1) spinel phases were associated with the 2 $MgO \cdot SiO_2$ phase (Figure 10).

The interior was a mixture of MgO, 2 MgO SiO_2, and $Mg(Al,Cr,Fe)_2O_4$ spinel with Al/Cr/Fe ratio of 3/3/2. Some of this spinel phase was found as small dendrites in the MgO phase.

3.2.1.4 2-2 (HM-1) 1668 to 1723K. Very little slag coated the brick surfaces; however, the slag had reacted with all the RFG leaving multiphase structure with no residual RFG structure (Figure 11). The two major phases were large crystalline particles of Mg rich $Mg(Al,Cr,Fe)_2O_4$ spinel with Al/Cr/Fe ratios near 4/1/1. The continuous phase was either vitreous or crystalline $CaO \cdot Al_2O_3 \cdot 2SiO_2$. This latter phase contained crystalline stringers of 2 $MgO \cdot SiO_2$ with smaller particles of high iron spinel $Mg(Fe,Al)_2O_4$ with Fe/Al ration of $\sim$3/1. It thus appears that near 1700°K or above, all the MgO in the original RFG has reacted with the slag forming some stable phases different from those formed at lower temperatures. The high Al, $Mg(Al,Cr,Fe)_2O_4$ appears to be the stable crystalline phase in a vitreous or crystalline $CaO \cdot Al_2O_3 \cdot SiO_2$ instead of the $MgO \cdot 2CaO \cdot 2SiO_2$ found at the lower temperatures. The 2 $MgO \cdot SiO_2$ (forsterite) phase, which was so prominent at the lower temperatures, was found only in the stringers within the anorthite.

3.2.2 Conclusions

At temperatures below $\sim$1700K, the MgO phase in the RFG is attacked by the silicon of the slag forming 2 $MgO \cdot SiO_2$ (forsterite) and a $MgO \cdot 2CaO \cdot 2SiO_2$ (akermanite) crystalline phase in a Ca rich Si depleted slag. The $Mg(Al,Cr,Fe)_2O_3$ spinel solid solution does not react with the silicate but may be a sink for some of the Al in the slag. As the operating temperature of the core increases, the chromium content of this phase appears to decrease suggesting general overall loss of Cr while the iron remains nearly constant. The amount of 2 $MgO \cdot SiO_2$ at the interface increases as the temperatures

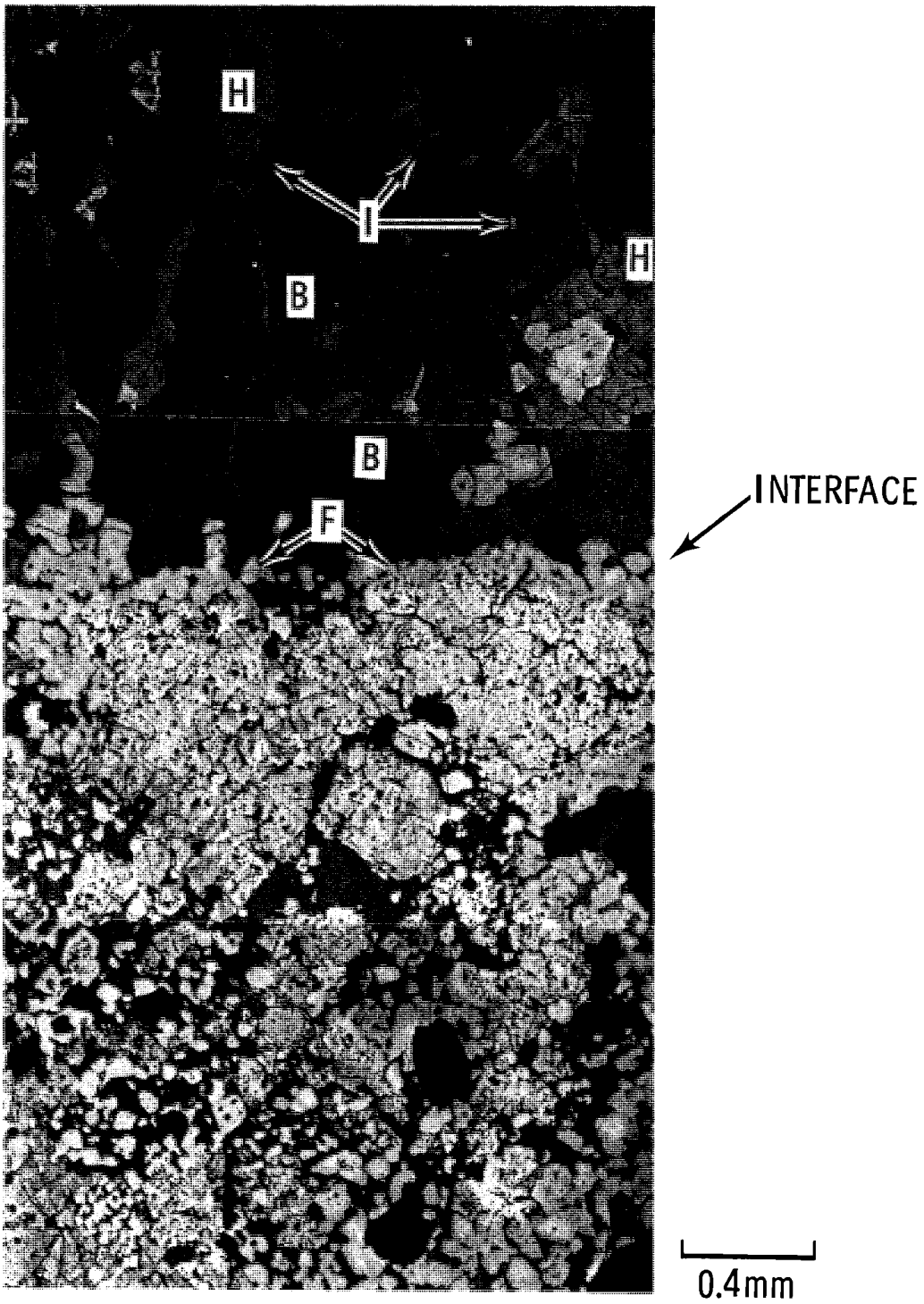

FIGURE 9. Microstructure of slag-RFG interface for 5-2 (HM-2) after testing at 1630-1683K. See Table 5 for notations.

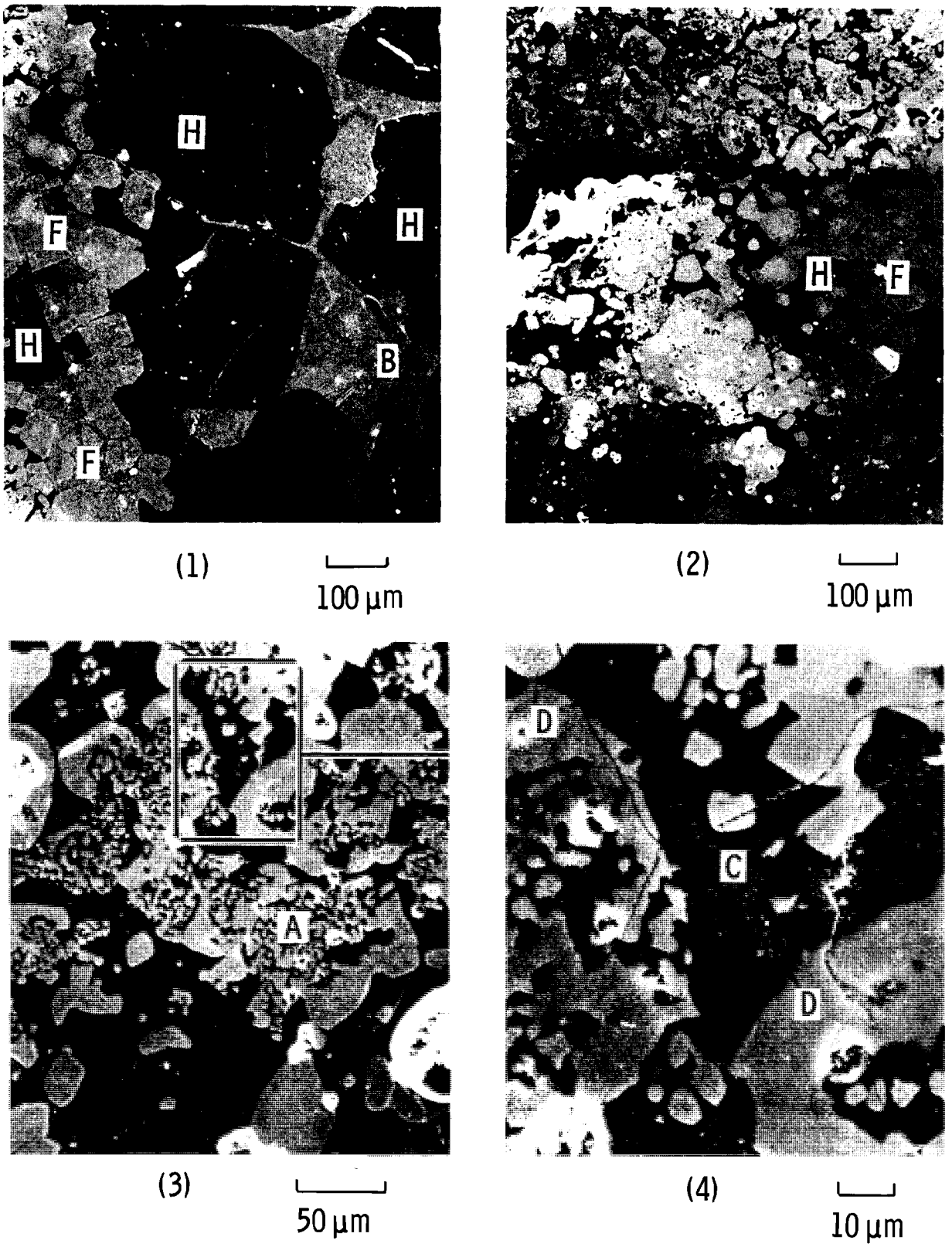

FIGURE 10. SEM microstructure of RFG 5-2 (HM-2) tested at 1630-1683K. See Table 5 for notations.

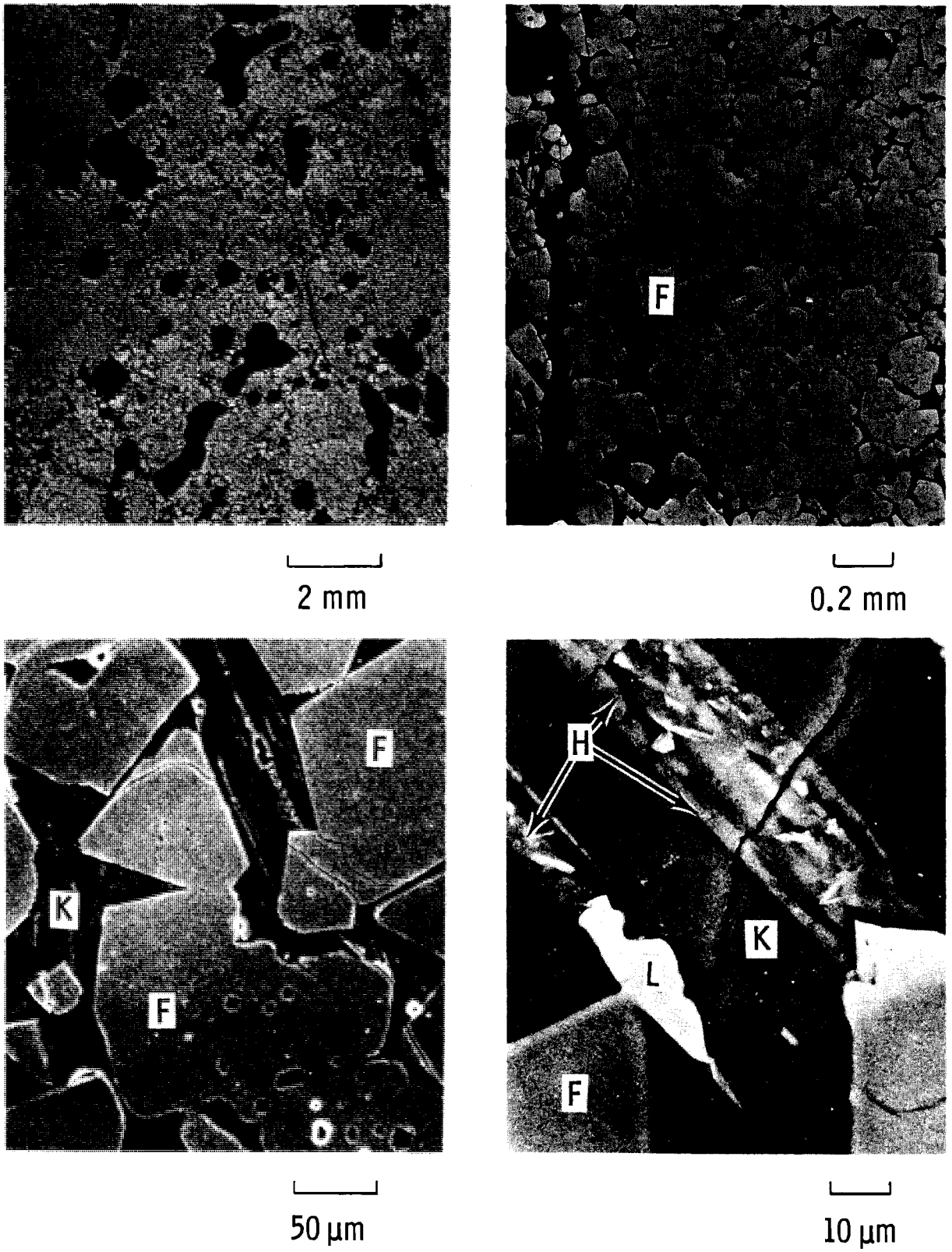

FIGURE 11. Microstructure of RFG-2 (HM-1) tested at 1668-1723K. See Table 5 for notations.

increase while the slag content decreases. The $Mg(Al,Cr,Fe)_2O_4$ phase also increases as the core temperature increases. However, overall there appears to be an overall loss of Mg in the RFG, expecially above 1600K. The amount of residual, unreacted RFG also decreases as the core temperature increases.

Above ∿1700K, the akermanite ($MgO_2 \cdot CaO \cdot 2SiO_2$) does not occur but is replaced by $CaO \cdot Al_2O_3 \cdot 2SiO_2$ (anorthite) which surrounds the crystalline $Mg(Al,Cr,Fe)_2O_3$. The forsterite, $2MgO \cdot SiO_2$ phase, so prevalent at the lower temperature, is observed only in long stringers in the anorthite.

Analysis of the larger slag particles which were removed from the bed or collected from the bottom of the bed after high temperature clean-out procedures, contained mixtures of similar slag phases, i.e. $2\ MgO \cdot SiO_2$ and $CaO\ Al_2O_3 \cdot 2SiO_2$ and some spinel solution.

Since the MgO appears to be the more susceptible phase in RFG to attack by the slag, consideration should be given to methods to make the MgO less reactive or to reduce its presence in the ceramic and increasing the spinel phase. MgO refractories have been made more resistant to silicate attack by adding Ca. In magnesia refractories, excess CaO is added to lower the solid solubility of SiO_2 by reducing the formation of low melting intergranular silicates. If RFG is considered further, such considerations must be made.

The effect of potassium in the combustion gas must also be considered, since in most slags associated with MHD, the potassium can be dissolved in the slag or react directly with the refractory. For example, the $K_2O \cdot Al_2O_3 \cdot 2SiO_2$, $K_2O \cdot 2SiO_2$, and $K_2O \cdot Al_2O_3 \cdot 4SiO_2$, etc., are generally formed in the condensed slag in MHD channels. This would strongly influence the corrosion reactions of the slag and alkali seed.

3.3 THERMAL AND ELECTRICAL PROPERTIES

The critical thermal and electrical properties of MHD materials are being measured in conjunction with the development, characterization, and testing of materials. Areas of present concern involve:

- Thermal diffusivity/conductivity of hafnium-rare earth oxides prepared in this laboratory for testing in Westinghouse's MHD Materials Test Facility (WESTF-42).
- Thermal diffusivity/conductivity of Y_2O_3 and CeO_2 stabilized ZrO_2 prepared by Westinghouse for testing in WESTF-42.
- Thermal diffusivity/conductivity of $SrZrO_3 \cdot Sr_xLa_{1-x}FeO_3$ prepared by MIT for possible MHD testing.

The methods for measuring thermal diffusivity and calculating the thermal conductivity have been described previously in detail.[5-6]

3.3.1 Thermal Diffusivity/Conductivity Hafnium-Rare Earth Oxides

The thermal diffusivity was measured and thermal conductivity calculated for the hafnium-rare earth oxides initially selected for further testing in simulated and actual MHD generators (see Section 3.1). The thermal diffusivity/conductivity as a function of temperature is required for the channel design. Therefore, in preparation for testing in Westinghouse's MHD Material Test Facility, the thermal diffusivity of these potential hafnium-rare earth oxides were measured using samples prepared prior to the fabrication of the actual sample to be used in WESTF-42. Subsequent measurements will be made on sibling samples prepared for the MHD test. Measurements were made on a number of samples prepared using different methods (Table 6).

The thermal conductivity is calculated from the product of the thermal diffusivity, specific heat, and density. Specific heat data are not available for these compositions, or even similar compositions. Values were calculated using Knoop-Neumann theory of mixtures and measured C_p values for the separate rare earth oxides and HfO_2.

TABLE 6. Compositions of Rare Earth-Hafnium Oxide Electrode Materials

Type A: $0.28PrO_2 \cdot 0.48Yb_2O_3 \cdot 0.66HfO_2$

A-17 - Sintered

3A-1245 - Sintered

M-158 - Hot Pressed

Type B: $0.063Tb_4O_7 \cdot 0.063Y_2O_3 \cdot 0.0874HfO_2$

B-1 - Sintered

M-159 - Hot Pressed

The specific heats for PrO_2 and Tb_4O_7 have not been measured. For Er_2O_3 only data from room temperature and below is reported. Therefore, since many properties of the rare-earth oxides are similar, C_p for other rare-earth oxides, adjacent in the periodic table to the one in question, were used when available. The specific heat data for CeO_2, Dy_2O_3, and Yb_2O_3 were used for PrO_2, Tb_4O_7, and Er_2O_3 respectively. The room temperature C_p for Yb_2O_3 was only a few percent different from that for the reported C_p for Er_2O_3. The heat capacity equations for these oxides are given in Table 7. Equations were developed where tabulated data were given in the references to allow a more accurate extrapolation to higher temperatures when necessary.

$$C_p = a + bT + CT^{-2} \text{ (cal/g - K)} \qquad (1)$$

The calculated heat capacities represent the largest underterminate error. Previous calculated values for oxides where actual C_p data were available indicate errors of $\sim$5% between the two values.

The density was measured geometrically and by water immersion with corrections made for temperature using a thermal expansion coefficient.

$$\frac{\Delta L}{L} \simeq 10.5 \times 10^{-6}/K \qquad (2)$$

This value was determined from previous measurements on similar compositions

and appear to vary only slightly from this value. Total errors introduced by this assumption are less than 1%.

The thermal diffusivity and thermal conductivity data are tabulated in Tables 8-12 and Figures 12,13. Data at higher temperatures were complicated above 1600°K because the sample reacted with the α-Al_2O_3 holder.

TABLE 7. Specific Heats of Oxides

Oxide	Specific Heat (C_p=a+b(K)+c(K^{-2})cal/g-K) a (10^{-2})	b (10^{-6})	c (10^{2})	Reference
HfO_2	8.262	9.881	-16.53	(7,8)
Y_2O_3	12.817	9.095	-19.393	(8)
Yb_2O_4	7.480	6.343	-4.871	(9)
CeO_2	9.689	13.41	-13.87	(8)
Dy_2O_3	7.725	9.314	-	(8)
$0.286PrO_2 \cdot 0.091Yb_2O_3 \cdot 0.667HfO_2$	8.450	11.336	-14.311	calc.
$0.06Tb_4O_7 \cdot 0.06Y_2O_3 \cdot 0.88HfO_2$	8.394	10.780	-13.964	calc.

TABLE 8. Data Sheet: Thermal Diffusivity/Conductivity

MHD Material: $0.286PrO_2 \cdot 0.048Yb_2O_3 \cdot 0.667HfO_2$

Source: Battelle Northwest (A-17)

Fabrication: Sintered 1875°K for 20 hr in air

Structure:

Heat Treatment: None

Density: 8.78 g/cm^3

Atmosphere: Argon

Property Data:

Temperature K	Thermal Diffusivity[1] m^2/sec (10^{-7})	Thermal Conductivity[2] Watts/m-K
588	4.252	1.33
753	4.545	1.47
953	4.674	1.57
1144	5.525	1.89
1377	5.302	1.86
1481	7.349	2.59
1319	4.836	1.57
1155	4.235	1.36
917	4.432	1.38
690	4.144	1.23

(1) $\Delta L/L - 10.5 \times 10^{-6} (\Delta K)$

(2) $C_p = 8.450 \times 10^{-2} + 1.133 \times 10^{-5} K - 1.431 \times 10^{3} K^{-2}$ (cal/g-K)

TABLE 9. Data Sheet: Thermal Diffusivity/Conductivity

MHD Material: $0.286PrO_2 \cdot 0.048Yb_2O_3 \cdot 0.666HfO_2$

Source: BNW (3A-1245)

Fabrication: Sintered at 1875°K for 20 hours in air

Structure:

Heat Treatment: None

Density: 9.50 g/cm^3

Atmosphere: Argon

Property Data:

Temperature K	Thermal Diffusivity (1) m^2/sec (10-7)	Thermal Conductivity (3) Watts/m-K
725	5.772	1.68
920	5.685	1.71
1116	6.545	2.01
1327	8.133	2.56
1506	13.845	4.41
1689 (2)	11.742	3.79

(1) $\Delta L/L - 10.5 \times 10^{-6} (\Delta K)$

(2) Sample reacted with Al_2O_3 sample holder

(3) $C_p = 8.450 \times 10^{-2} + 1.133 \times 10^{-5} K - 1.431 \times 10^{3} K^{-2}$ (cal/g-K)

TABLE 10. Data Sheets: Thermal Diffusivity/Conductivity

MHD Material: $0.29PrO_2 \cdot 0.05Yb_2O_3 \cdot 0.66HfO_2$

Source: BNW Powder--Fabricated Westinghouse Research (HO-BN 0201) (M-158)

Fabrication: Hot pressed at 1873°K at 27.6 MPa (4000 psi)

Structure:

Heat Treatment: None

Density: 8.82 g/cm^3

Atmosphere: Argon

Property Data:

Temperature K	Thermal Diffusivity[1] m^2/sec (10^{-7})	Thermal Conductivity[2] Watts/m-K
474	1.048	2.94
714	1.087	3.29
929	1.365	4.27
1099	1.289	4.11
1307	1.245	4.04
1532	0.829	2.74
1418	0.959	3.15
1219	0.983	3.16
1042	0.944	2.99
861	1.066	3.31
685	1.064	3.20
489	1.002	2.83

(1) $\Delta L/L = (10.5 \times 10^{-6})\ \Delta K$

(2) $C_p = 8.450 \times 10^{-2} + 1.133 \times 10^{-5} K - 1431 \times 10^{3} K^{-2}$ (cal/g-K)

TABLE 11. BNW Data Sheet: Thermal Diffusivity/Conductivity

MHD Material: $0.063Tb_4O_7 \cdot 0.063Y_2O_3 \cdot 0.875HfO_2$

Source: Battelle-Northwest (B-1)

Fabrication: Sintered at 1875°K for 20 hours in air

Structure:

Heat Treatment: None

Density: 8.96 g/cm^3

Atmosphere: Argone

Property Data:

Temperature K	Thermal Diffusivity[1] m^2/sec (10^{-7})	Thermal Conductivity[2] Watts/m-K
670	7.476	2.30
840	6.880	2.19
1008	6.685	2.17
1206	7.424	2.46
1437	7.115	2.40
1511	7.187	2.44
1322	7.173	2.40
1166	8.087	2.67
966	7.718	2.49
763	7.853	2.46
560	9.413	2.81

(1) $\Delta L/L - 10.5 \times 10^{-6} (\Delta K)$

(2) $C_p = 1.282 \times 10^{-1} + 9.095 \times 10^{-6} K - 1.939 \times 10^{3} K^{-2}$ (cal/g-K)

TABLE 12. Data Sheet: Thermal Diffusivity/Conductivity

MHD Material: $0.063Tb_4O_7 \cdot 0.063Y_2O_3 \cdot 0.875HfO_2$

Source: BNW Powder--Hot Pressed Westinghouse (M-159) HO-BN-1010

Fabrication: Hot pressed at 1675°K at 27.6 MPa (4000 psi)

Structure:

Heat Treatment: None

Density: 8.88 g/cm^3

Atmosphere: Argon

Property Data:

Temperature K	Thermal Diffusivity(1) m^2/sec (10^{-7})	Thermal Conductivity(2) Watts/m-K
491	5.787	1.66
713	5.247	1.61
938	4.727	1.51
1118	4.810	1.56
1329	5.021	1.67
1517	4.769	1.61
1422	4.804	1.61
1245	4.840	1.60
1046	4.907	1.58
852	5.222	1.65
636	5.284	1.60

(1) $\Delta L/L = 10.5 \times 10^{-6} (\Delta K)$

(2) $C_p = 1.282 \times 10^{-1} + 9.095 \times 10^{-6}K - 1.939 \times 10^{3}K^{-2}$ (cal/g-K)

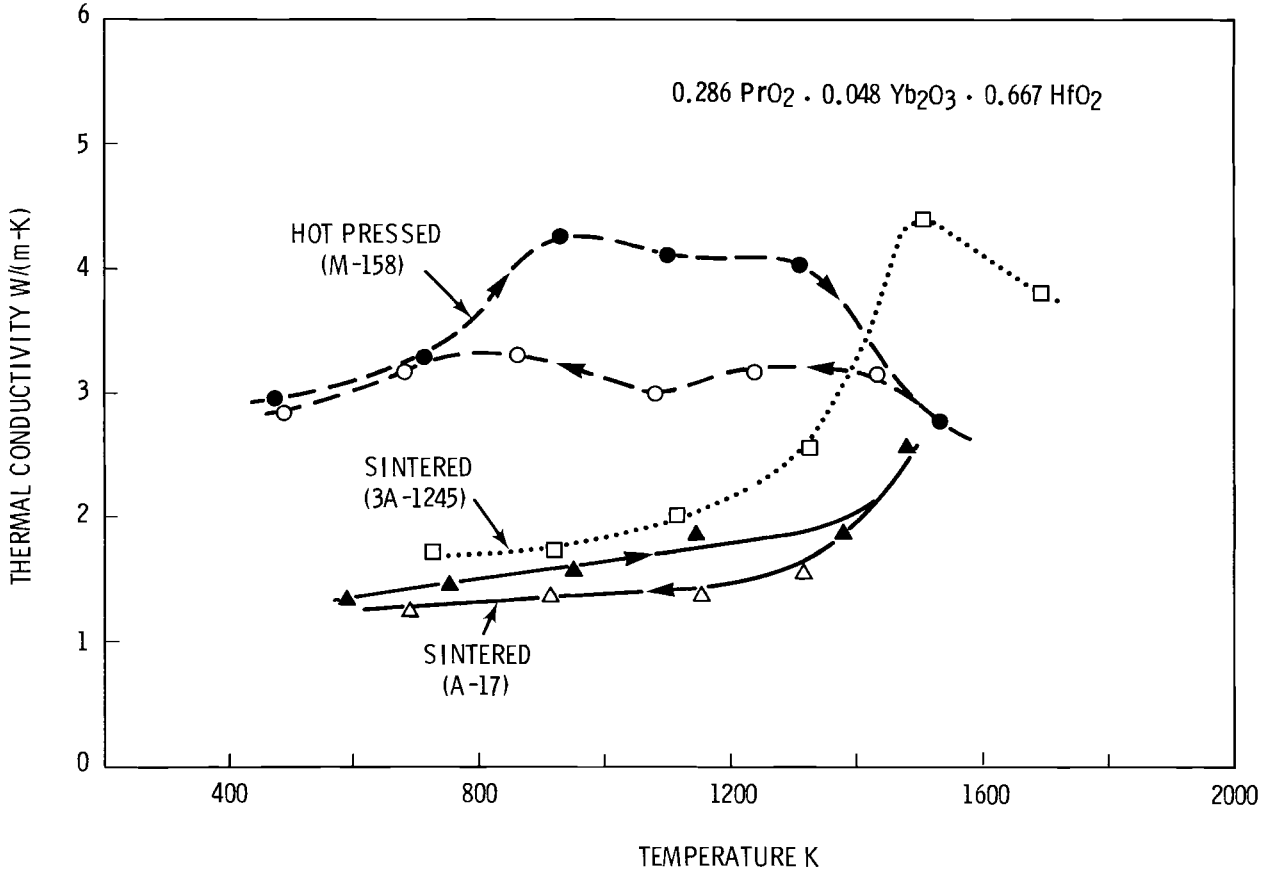

FIGURE 12. Thermal Conductivity of $0.286PrO_2 \cdot 0.048Yb_2O_3 \cdot 0.667HfO_2$.

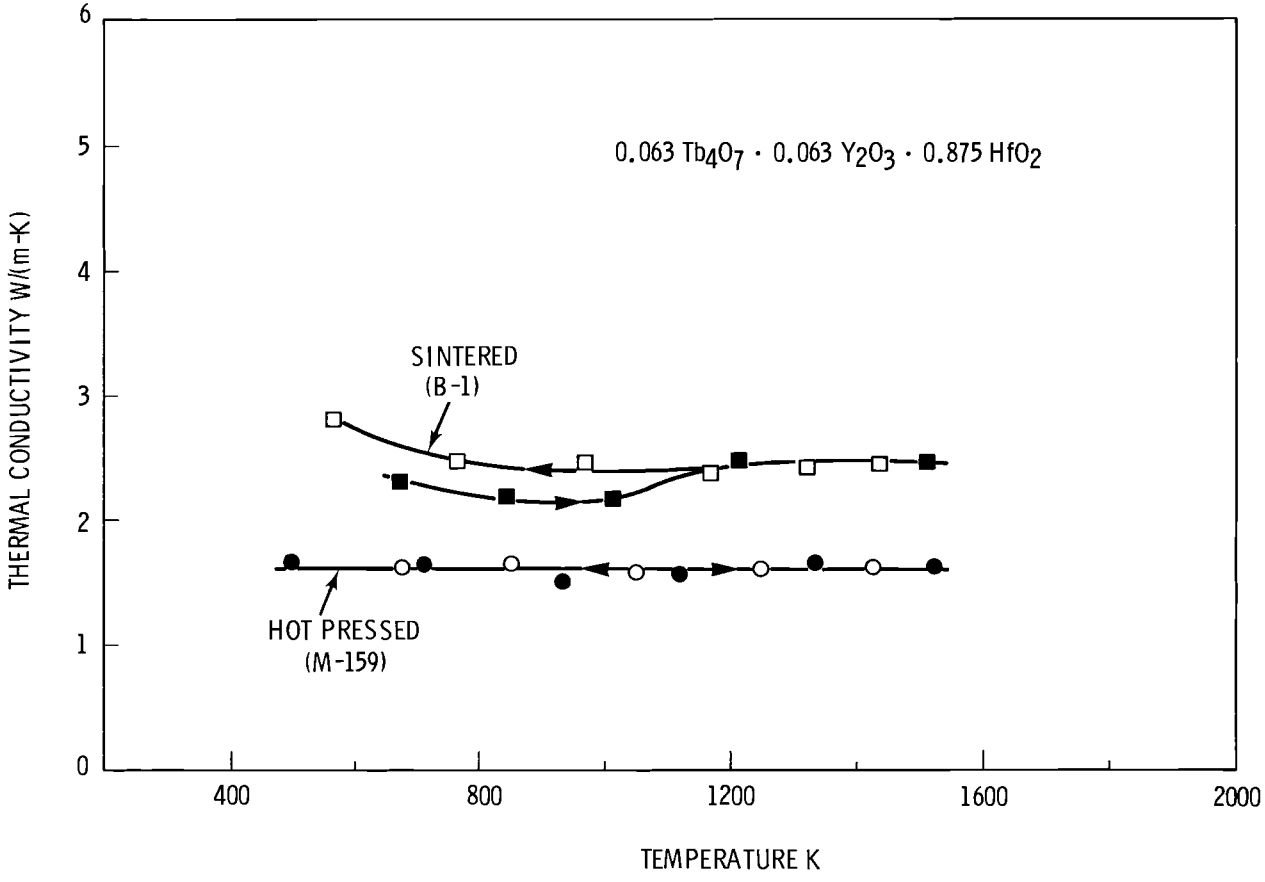

FIGURE 13. Thermal Conductivity of $0.063Tb_4O_7 \cdot 0.063Y_2O_3 \cdot 0.87HfO_2$.

The thermal conductivities of the $0.286PrO_2 \cdot 0.048Yb_2O_3 \cdot 0.667HfO_2$ changed significantly with temperature and on heating and cooling, Figure 12. The hot pressed sample (M-158) exhibited a large increase near 800-900K with subsequent decrease near 1300-1400K. On cooling, the conductivity was less temperature dependent with a constant value $\sim$3 W/(m-K). The increase near 800-900°K could have resulted from annealing of stress introduced during pressing. There was, however, a significant change observed in the microstructure on heating, Figure 14, with the formation of small pores (up to 1 μm) and microcracks (up to 0.1 mm long). This was probably the cause of the permanent decrease on cooling for the hot pressed sample. The sintered samples exhibited an increase in conductivity between 1300-1400K. The sintered sample (A-17) did not change microstructure, Figure 15. The 3A-1245 sample heated to higher temperatures had reacted with the Al_2O_3 making structural comparison after the measurements difficult, Figure 15. This increase could be related to possible phase changes which could be anticipated on this unknown complex ternary phase system. Further measurements to higher temperatures will be made.

The thermal conductivity for $0.063Tb_4O_7 \cdot 0.63Y_2O_3 \cdot 0.875HfO_2$ was nearly temperature independent, exhibiting essentially the same values on heating and cooling. No change in microstructure was observed after heating in either sample. The difference between the two samples is attributed to differences in the microstructure, with M-159 hot press samples being multiphase, Figure 16.

The thermal diffusivity of these sample compositions will be re-measured using sibling compacts fabricated for testing in WESTF-42. Higher temperature data will be obtained using the $ZrO_2(Y_2O_3)$ sample holder.

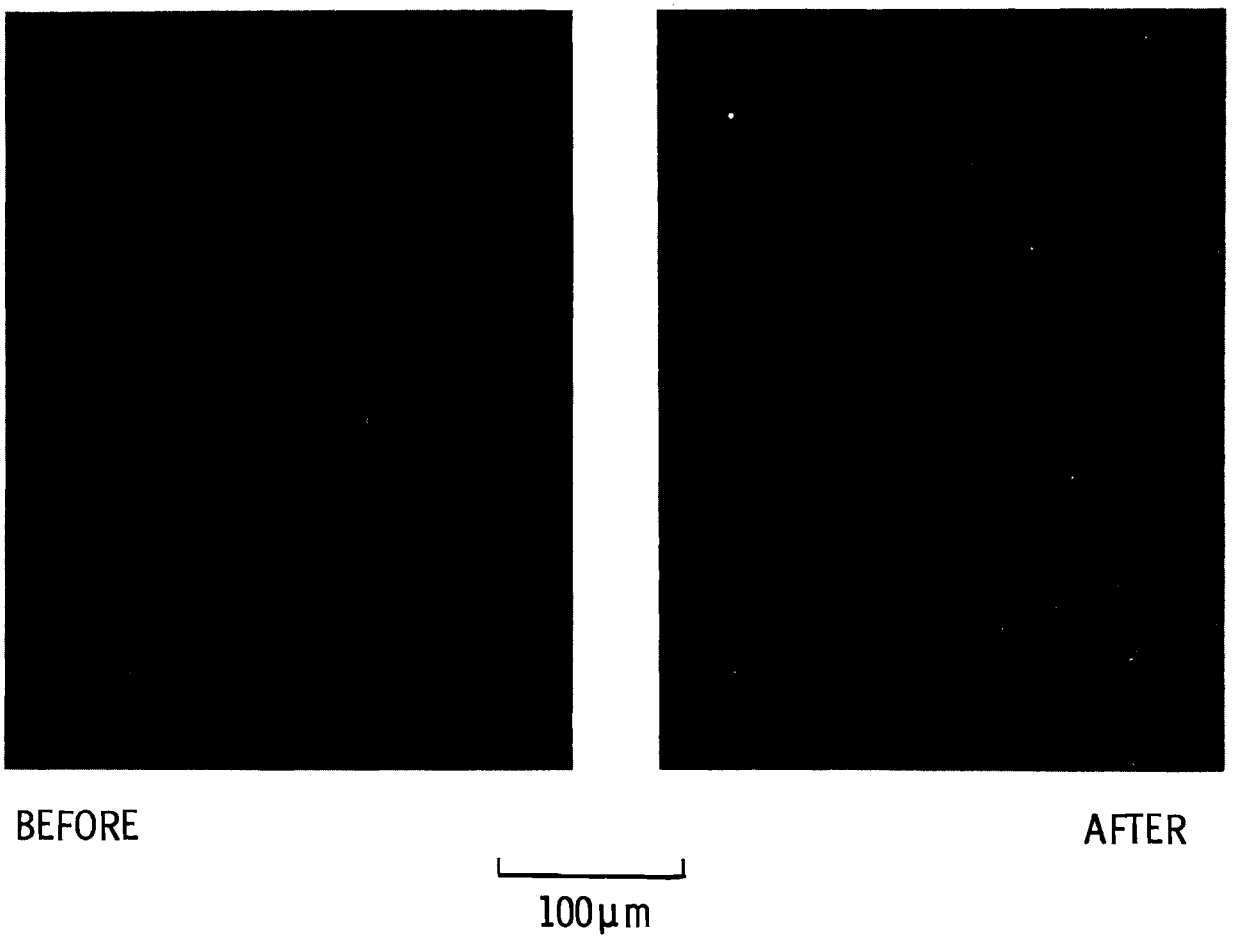

FIGURE 14. Microstructure of Hot Pressed $0.286PrO_2 \cdot 0.048Yb_2O_3 \cdot 0.667HfO_2$ [M-158] Before and After Testing.

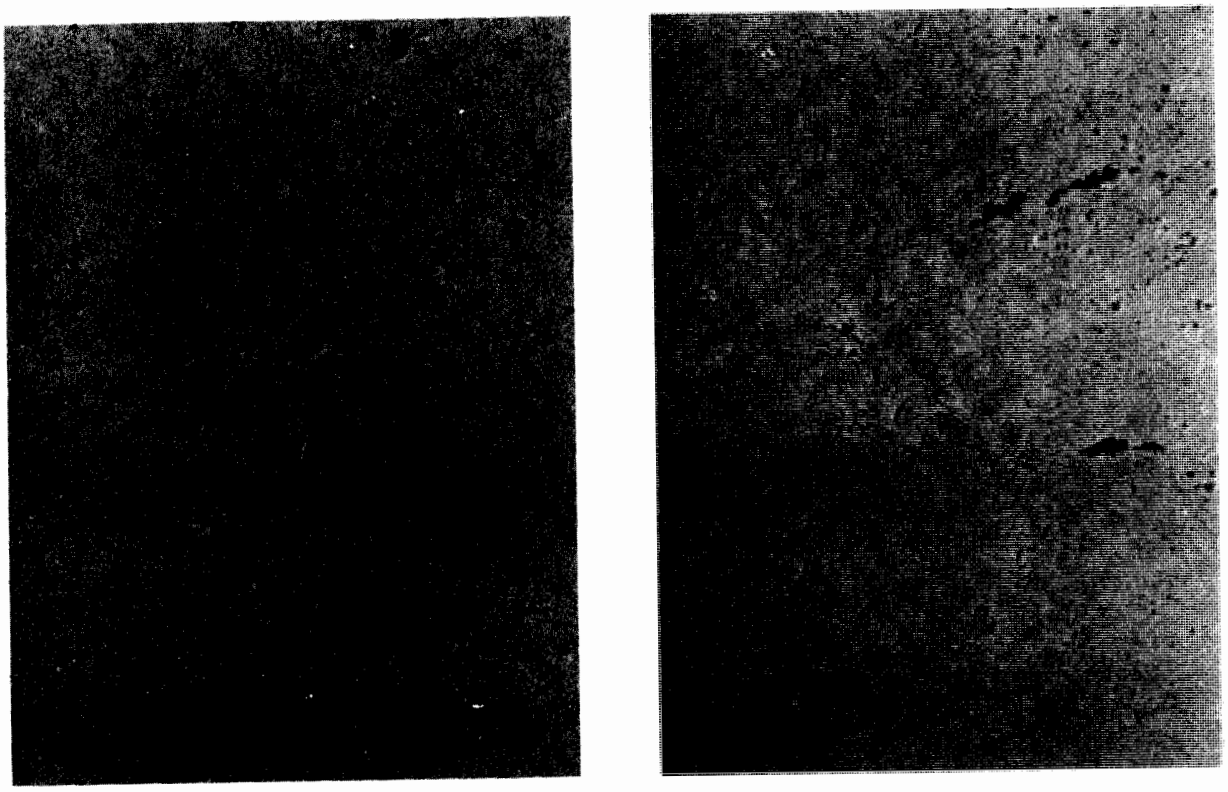

FIGURE 15. Microstructure of $0.286PrO_2 \cdot 0.048Yb_2O_3 \cdot 0.667HfO_2$ [A-17] and [A-12345].

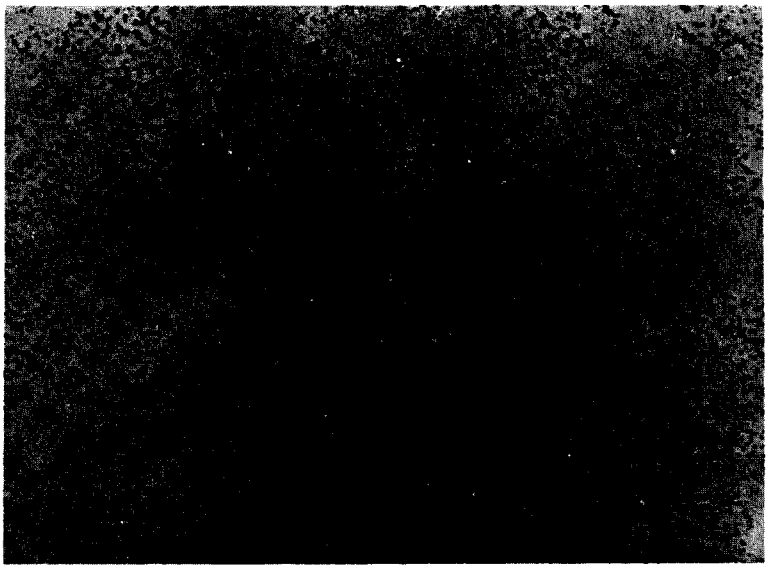

FIGURE 16. Microstructure of $0.036Tb_4O_7 \cdot 0.063Y_2O_3 \cdot 0.875HfO_2$ [MN-159].

3.3.2 Thermal Diffusivity/Conductivity Yttrium or Calcium Magnesium Oxide Stabilized Zirconium Oxides

The thermal diffusivity measured and thermal conductivity calculated for three Y_2O_3 or CaO stabilized ZrO_2 electrode materials to be tested in the Westinghouse MHD Materials Test Facility, WESTF-42 included:

- $0.12Y_2O_3 \cdot 0.88ZrO_2$ [M-154]
- $0.12Y_2O_3 \cdot 0.88ZrO_2$ [heat treated M-155]
- $0.15[Mg_{0.625}Ca_{0.375}]O \cdot 0.85ZrO_2$ [M-156]

The M-154 sample was identical to the electrode material tested by the U.S. in the USSR U-02 MHD facility.[10]

The heat capacity for all three materials was assumed to be the same. Data for $0.12Y_2O_3 \cdot 0.88ZrO_2$ has been measured and has been fit to the equation

$$C_p = 0.1228 + 2.860 \times 10^{-5}K - 1.905 \times 10^{3}K^{-2} (cal/g\text{-}K)$$

The density was corrected for thermal expansion using previously measured values[10-11] with $\Delta L/L = 12 \times 10^{-6}$.

The thermal diffusivity and thermal conductivity data are tabulated in Tables 13-15, and summarized in Figure 17. The conductivities are relatively temperature dependent, with some waviness. The $0.15(Mg_{0.625}Ca_{0.375})O\ 0.85ZrO_2$ also exhibited some hysteresis on heating and cooling. The values for the $0.12Y_2O_3 \cdot 0.88ZrO_2$ samples, M-154 and M-155, differ with the latter values very close to the M-155 sample. The M-155 and U-02 Phase I sample had very similar densities, 4.82 g/cm^3 (83.3%TD) and 4.85 g/cm^3 (82.2%TD), respectively. These densities were substantially lower than the M-156 sample, 5.19 g/cm^3 (88.0%TD). It has been shown previously with these materials that the thermal

TABLE 13. BNW Data Sheet: Thermal Diffusivity/Conductivity

MHD Material: $0.12Y_2O_3 \cdot 0.88ZrO_2$

Source: Westinghouse Research Center, U-02 Phase I (M-154)

Fabrication: Sintered 1873°K in air

Structure:

Heat Treatment: 2173°K for 2 hours

Density: 5.19 g/cm^3

Atmosphere: Argon

Property Data:

Temperature K	Thermal Diffusivity(1) m^2/sec (10^{-7})	Thermal Conductivity(1,2) Watts/m-K
682	5.132	1.54
870	5.800	1.80
1023	4.966	1.63
1232	5.202	1.71
1480	4.848	1.71
1567	4.720	1.62

(1) $\Delta L/L = 12 \times 10^{-6}$

(2) $C_p = 0.1227 + 2.860 \times 10^{-5}K - 1.945 \times 10^{3}K^{-2}$ cal/g-K(10)

TABLE 14. BNW Data Sheet: Thermal Diffusivity/Conductivity

MHD Material: $0.12Y_2O_3 \cdot 0.88ZrO_2$

Source: Westinghouse Research Center [M-155)

Fabrication: Sintered

Structure:

Heat Treatment: 2173°K in air

Density: 4.92 g/cm^3

Atmosphere: Argon

Property Data:

Temperature K	Thermal Diffusivity(1) m^2/sec (10^{-7})	Thermal Conductivity(1.2) Watts/m-K
634	4.346	1.22
866	4.211	1.24
1053	3.924	1.18
1237	3.985	1.24
1395	3.693	1.17
1606	3.591	1.18
1605	3.360	1.10
1379	3.559	1.13
1190	3.794	1.17
950	3.723	1.11
611	4.241	1.19

(1) $\Delta L/L = 12 \times 10^{-6}$

(2) $C_p = 0.1227 + 2.8600 \times 10^{-5}K - 1.945 \times 10^{3}K^{-2}$ (cal/g-K)

TABLE 15. BNW Data Sheet: Thermal Diffusivity/Conductivity

MHD Material: $0.15(Mg_{0.625}Ca_{0.375})O \cdot 0.85ZrO_2$

Source: Westinghouse Research Center (M-156)

Fabrication: Sintered

Structure:

Heat Treatment: 2173K in air

Density: 5.02

Atmosphere: Argon

Property Data:

Temperature K	Thermal Diffusivity(1) m^2/sec (10^{-7})	Thermal Conductivity (1,2) Watts/m-K
705	5.214	1.587
912	5.942	1.871
1087	5.876	1.887
1289	5.300	1.724
1473	5.150	1.702
1629	4.812	1.592
1531	4.870	1.609
1359	4.762	1.561
1190	4.965	1.619
921	4.844	1.533
683	4.995	1.511

(1) $\Delta L/L = 12 \times 10^{-6}$

(2) $C_p = 0.1227 + 2.8600 \times 10^{-5}K - 1.945 \times 10^{3}K^{-2}$ (cal/g-K)

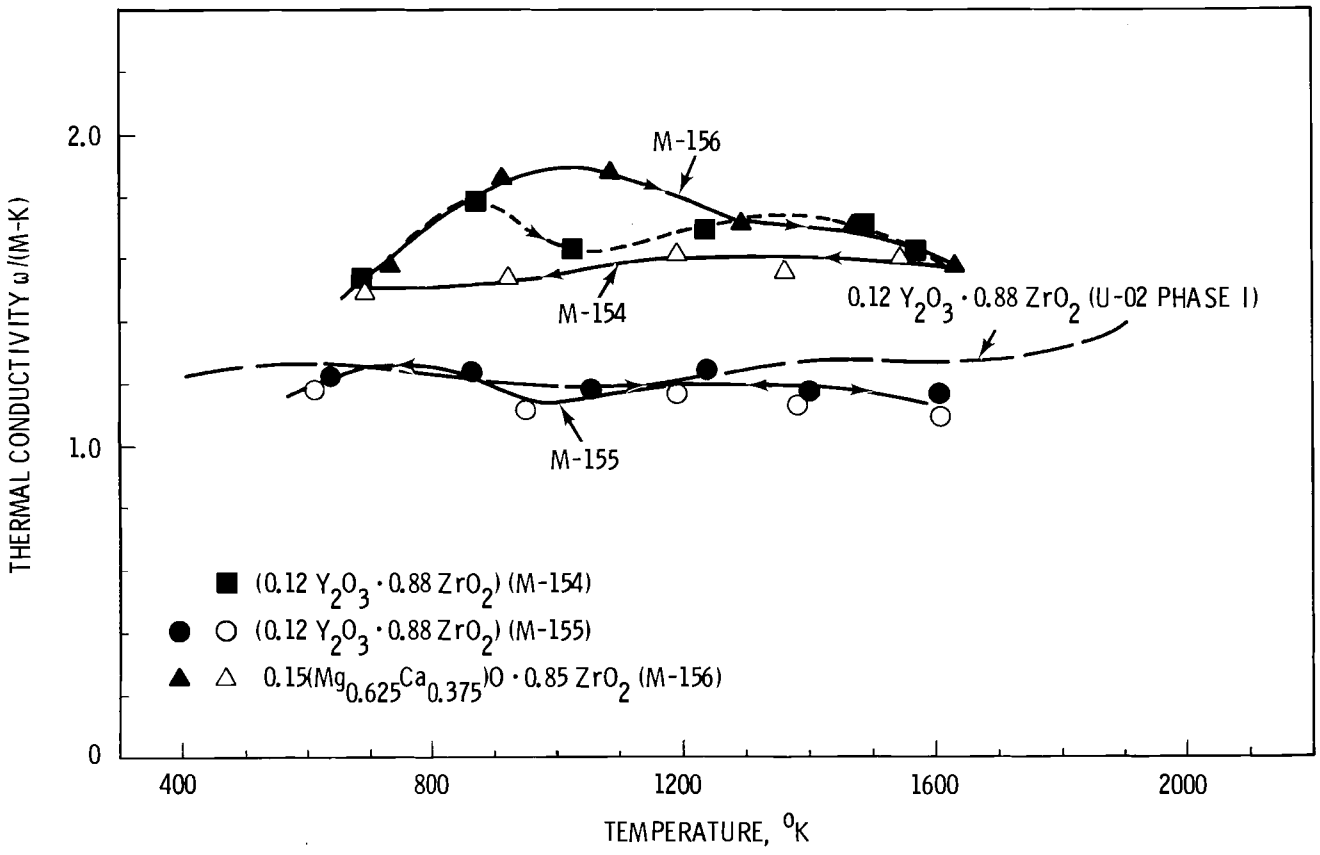

FIGURE 17. Thermal Conductivity of $0.12Y_2O_3 \cdot 0.88ZrO_2$ [M-154 and M-155], and $0.15(Mg_{0.625}Ca_{0.375})O \cdot 0.85ZrO_2$ [M-156].

conductivity is strongly dependent upon the percent of open porosity.[12] If the ∿5% difference in density represents primarily open porosity differences, this could easily explain the ∿33% higher conductivity of the M-154 sample. These previous results indicate a large increasing conductivity with decreasing open porosity. A similar analogy could be made for the $0.15(Mg_{0.625}Ca_{0.375})O \cdot 0.85ZrO_2$ (M-156) sample which also had a higher theoretical density (88%) and assumed lower open porosity. However, some open porosity data was not available for these samples and analytical evaluation could not be made.

4.0 ANTICIPATED ACCOMPLISHMENTS NEXT QUARTER

4.1 DEVELOPMENT AND FABRICATION

Electrodes of the hafnium-rare-earth oxides will be fabricated and prepared for testing (November 1979) in the Westinghouse MHD Materials Test Facility (WESTF-42). Four compositions will be prepared for this thermal-slag test.

Development of a graded hafnium-rare-earth oxide electrode with a high temperature refractory surface and a lower temperature, highly electrically conducting current leadout, for attachment to cold copper base will continue. The present development includes use of a $HfO_2 \cdot R_2O_3 \cdot In_2O_3$ ternary as the oxide current leadout. The fabrication procedures for this graded oxide electrode will be developed. Electrodes will be fabricated for testing in WESTF under thermal and MHD conditions in the first quarter 1980.

4.2 CHARACTERIZATION AND EVALUATION

4.2.1 Properties

The evaluations of the thermal and electrical properties of potential electrode materials will continue. This will include the critical data for $HfO_2 \cdot R_2O_3$ electrodes and $0.5SrZrO_3 \cdot 05(Sr,La)FeO_3$ which are being considered for design and testing in WESTF.

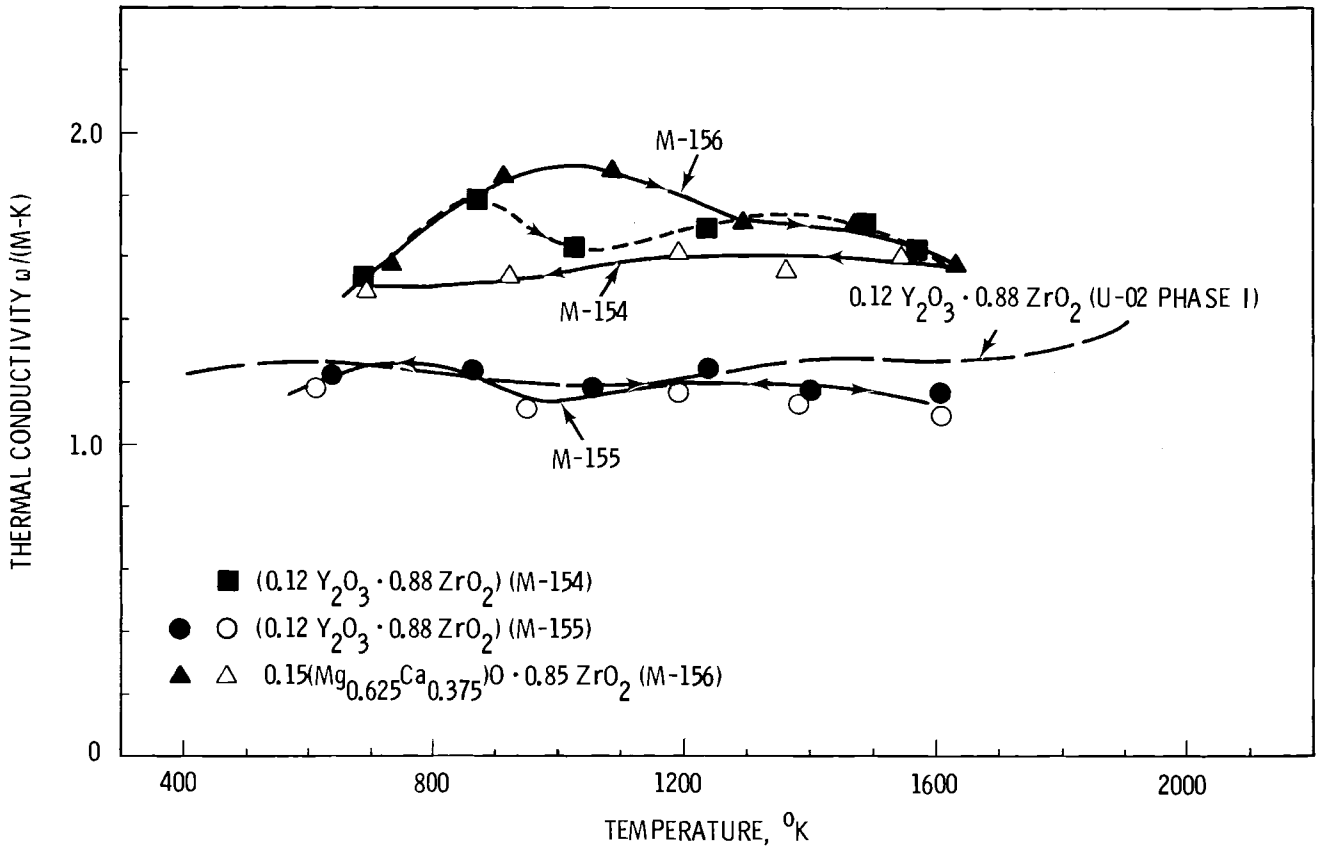

FIGURE 17. Thermal Conductivity of $0.12Y_2O_3 \cdot 0.88ZrO_2$ [M-154 and M-155], and $0.15(Mg_{0.625}Ca_{0.375})O \cdot 0.85ZrO_2$ [M-156].

conductivity is strongly dependent upon the percent of open porosity.[12] If the ∿5% difference in density represents primarily open porosity differences, this could easily explain the ∿33% higher conductivity of the M-154 sample. These previous results indicate a large increasing conductivity with decreasing open porosity. A similar analogy could be made for the $0.15(Mg_{0.625}Ca_{0.375})O \cdot 0.85ZrO_2$ (M-156) sample which also had a higher theoretical density (88%) and assumed lower open porosity. However, some open porosity data was not available for these samples and analytical evaluation could not be made.

4.0 ANTICIPATED ACCOMPLISHMENTS NEXT QUARTER

4.1 DEVELOPMENT AND FABRICATION

Electrodes of the hafnium-rare-earth oxides will be fabricated and prepared for testing (November 1979) in the Westinghouse MHD Materials Test Facility (WESTF-42). Four compositions will be prepared for this thermal-slag test.

Development of a graded hafnium-rare-earth oxide electrode with a high temperature refractory surface and a lower temperature, highly electrically conducting current leadout, for attachment to cold copper base will continue. The present development includes use of a $HfO_2 \cdot R_2O_3 \cdot In_2O_3$ ternary as the oxide current leadout. The fabrication procedures for this graded oxide electrode will be developed. Electrodes will be fabricated for testing in WESTF under thermal and MHD conditions in the first quarter 1980.

4.2 CHARACTERIZATION AND EVALUATION

4.2.1 Properties

The evaluations of the thermal and electrical properties of potential electrode materials will continue. This will include the critical data for $HfO_2 \cdot R_2O_3$ electrodes and $0.5SrZrO_3 \cdot 05(Sr,La)FeO_3$ which are being considered for design and testing in WESTF.

4.2.2 Electrodes

The characterization and evaluation of a Pt coated Cu anode tested in AVCO's Mark VII using K_2SO_4 as seed with slag will be completed. This will include an evaluation of the anode's corrosion of the slag/seed on both Pt and Cu.

The characterization of slags from Stanford University's MHD channel using Pt-Cu electrodes will continue.

4.2.3 Air Preheater Materials

The characterization and evaluation of a variety of refractories for potential in directly coal fired MHD air preheaters will continue. These materials were tested in Montana State University's heat exchanger. Also being studied are slags removed from this air preheater.

REFERENCES

1. J. Lambert Bates, Development, Characterization and Evaluation of Materials for Open Cycle MHD, Quarterly Report for the Period Ending June 1978, PNL-2004-8, Pacific Northwest Laboratory, Richland, Washington (1978).

2. J. Lambert Bates, Development, Characterization and Evaluation of Materials for Open Cycle MHD, Quarterly Progress Report for the Period Ending September 1978, PNL-2004-9, Pacific Northwest Laboratory, Richland, Washington (1978).

3. J. Lambert Bates and D. D. Marchant, Development, Characterization and Evaluation of Materials for Open Cycle MHD, Quarterly Report for the Period Ending December 1978, PNL-2004-10, Pacific Northwest Laboratory, Richland, Washington (1979).

4. S. L. Dole, R. W. Scheidecker, L. R. Shiers, M. F. Berard and O. Hunter, Jr., "Technique for Preparing Highly Sinterable Oxide Powders," Materials Science and Engineering, 32 p 277-281 (1978).

5. J. Lambert Bates, Thermal Conductivity of "Round Robin" Uranium Dioxide, BNWL-1431, Pacific Northwest Laboratory, Richland, Washington (1977).

6. J. Lambert Bates, Development, Characterization and Evaluation of Materials for Open Cycle MHD, Quarterly Progress Report, October - December 1976, BNWL-2004-5, Pacific Northwest Laboratory, Richland, Washington (1977).

7. Raymond Orr, "High Temperature Heat Contents of Hafnium Dioxide and Hafnium Tetrachloride," J. Am. Chem. Soc., 75, 1231-2 (1953).

8. Y. S. Touloukian, R. W. Powell, C. Y. Ho, and M. C. Nicolaou, Thermophysical Physical Properties of Matter, Vol. 5, Plenum Press. New York (1973).

9. D. Sh. Tsagareishvii and G. G. Gvelesiani, "Entholpies and Heat Capacities of Oxides of Rare-Earth Metals," Russ. J. Inorg. Chem., 10 (2), 171-2 (1965).

10. Wm. R. Hosler, ed., Joint US-USSR Test of US MHD Electrode Systems in USSR U-02 MHD Facility (Phase I), ERDA-76/154 (1976).

11. K. E. Wilkes and J. F. Lagedrost, Thermophysical Properties of Plasma Spray Coatings, NASA-CR-121144 (1973).

12. J. Lambert Bates and D. D. Marchant, "Thermal Properties of MHD Electrode Materials," 17th Symposium Engineering Aspects of Magnetohydrodynamics, pub. by Stanford University, Palo Alto, California, pp D.6.1-7 (1978).

DISTRIBUTION

No. of Copies

OFFSITE

Aerodyne Research, Inc.
Center for Chemical and
Environmental Physics
Bedford Research Park
Crosby Drive
Bedford, MA 01730
Attn: Dr. C. Kolb

Air Force Aero Propulsion Lab.
Aerospace Power Division
AFAPL/PO
Wright Patterson AFB, OH 45433
Attn: Mr. R. Cooper

5 Argonne National Laboratory
9700 S. Cass Avenue
Argonne, IL 60439
Attn: Dr. M. Petrick
Mr. E. G. Pewitt
Dr. E. Pearson
Dr. C. Redman
Dr. K. Kuczen

ARO, Inc.
AEDC Division
Arnold Air Force Station
TN 37389
Attn: Mr. Rogers F. Starr
PWT/PT

3 AVCO Everett Research Lab., Inc.
2385 Revere Beach Pkwy.
Everett, MA 02149
Attn: Dr. R. Detra
Mr. F. Hals
Dr. S. Petty

Central Mine Planning & Design
Institute, Ltd.
Gondwana Place
Kanke Rd.
Ranchi 834008 India
Att: Dr. R. P. Indwar

No. of Copies

Computer Sciences, Inc.
6565 Arlington Blvd.
Falls Church, VA 22046
Attn: W. Schlener

DYNATREND INCORPORATED
1911 N. Ft. Meyer Drive, Suite 907
Rosslyn, VA 22209
Attn: Mr. John A. Polutchko

DYNATREND INCORPORATED
21 Cabot Road
Woburn, MA 01801
Attn: Mr. B. Wasserman

2 Electric Power Research Institute
P. O. Box 10412
3412 Hillview Avenue
Palo Alto, CA 94303
Attn: Mr. A. C. Dolbec, Advanced Fossil
Power Systems (1 copy)
Paul Zieglebaum

FluiDyne Engineering Corp.
5900 Olson Memorial Highway
Minneapolis, MN 55422
Attn: Mr. D. DeCoursin

2 General Electric Co. Space Sciences Co.
Space Division, P.O. Box 8555
Philadelphia, PA 19101
Attn: Dr. R. Rosenberg
RM-9132
Mr. L. Terrey

Gilbert Associates, Inc.
P. O. Box 1498
Reading, PA 19603
Attn: Dr. J. Cutting

3 MIT/FBNML
170 Albany Street
Cambridge, MA 02139
Attn: Ms. Albe Dawson/NW14-2525
Dr. B. Montgomery/NW14-3211

No. of Copies

2 Massachusetts Institute of Technology
Dept. of Aeronautics & Astronautics
77 Massachusetts Avenue
Cambridge, MA 02139
Attn: Prof. J. F. Louis
Rm 31-254
H. Kent Bowen

Mississippi State University
Aerophysics and Aerospace Engineering
P. O. Drawer A/AP
Mississippi State, MS 29762
Attn: Dr. D. Murphree

Department of Mechanical Engineering
Montana State University
Bozeman, MT 59715
Attn: Dr. D. Blackketter

Montana College of Mineral Science and Technology
West Park Street
Butte, MT 59701
Attn: Dr. Bryce Rhodes

5 Montana Energy and MHD R&D Institute
Box 3890
Butte, MT 59701
Attn: Mr. J. D. Meglen
Dr. J. J. Rasmussen
Mr. D. Dolenc
Dr. E. O'Hair
Mr. B. Middleton

2 NASA/Lewis Research Center
21000 Brookpark Road
Cleveland, Ohio 44135
Attn: Mr. George Seikel,
Manager MHD Project Office-Mail Stop 500-202 (1 copy)
Dr. Robert Bercaw,
Assistant Manager, MHD Project Office-Mail Stop 500-202

1 Pittsburgh Energy Technology Center
4800 Forbes Avenue
Pittsburgh, PA 15213
Attn: Mr. D. Bienstock

No. of Copies

2 Polytechnic Institute of New York
Route 110
Farmingdale, NY 11735
Attn: Prof. Martin Bloom

Ralph M. Parsons Co.
100 West Walnut Street
Pasadena, CA 91124
Attn: Mr. R. Gibbons

Rand Corporation
2100 M Street NW
Washington, D.C. 20037
Attn: Dr. R. Y. Pei

3 Reynolds Metals Co.
P. O. Box 1200
Sheffield, AL 35660
Attn: Dr. E. P. Scannell,
Energy Conversion Division

Rockwell International
Rocketdyne Division
Energy Systems Group
8900 DeSoto Avenue
Canoga Park, CA 91304
Attn: Mr. C. A. Hauenstein
LA39 (1 copy)

Sandia Laboratories
P. O. Box 500
Albuquerque, NM 87115
Attn: Dr. F. G. Blottner/1261

Stanford University
Stanford, CA 94305
Attn: Dr. E. H. Eustis

2 STD Corporation
P. O. Box "C"
Arcadia, CA 91006
Attn: Mr. S. Demetriades
Mr. C. Maxwell

3 TRW
One Space Park
Redondo Beach, CA 90278
Attn: Mr. H. Graham
Mr. J. Hardgrove

No. of Copies

A. A. Churm
DOE Chicago Patent Group
9800 South Cass Avenue

2 U. S. Dept. of Commerce
National Bureau of Standards
Washington, D. C. 20234
Attn: Mr. Samuel Schneider

4 University of Tennessee Space Institute
Tullahoma, TN 37388
Attn: Dr. John B. Dicks, Director
Dr. Susan Wu
Energy Conversion Division
Dr. James Chapman,
Program Manager
Mr. Richard H. Smith,
Section Manager, Planning and Information Services
(1 copy)

4 Westinghouse Electric Corporation
Advanced Energy Systems Division
P.O. Box 10864
Pittsburgh, PA 15236
Attn: Mr. J. Sadler
Mr. F. Retallick
Mr. J. M. Feret

Westinghouse Electric Corporation
Research & Development Center
1310 Beulah Road
Pittsburgh, PA 15235
Attn: Dr. B. Rossing

3 Department of Energy
Division of MHD
ET-FE-MHD
Mail Stop 336
Washington, DC 20545
Attn: Marshall Sluyter
Steven Saks
George Rudins

27 DOE Technical Information Center

ONSITE

No. of Copies

2 DOE Richland Operations Office
H. E. Ransom
Program Office

39 Battelle-Northwest

J. L. Bates (20)
L. R. Bunnell
T. D. Chikalla (2)
J. L. Daniel
P. E. Hart
D. D. Marchant (2)
C. R. Hann
D. E. Olesen
L. C. Schmid/J. Cox
G. L. Tingey
R. P. Turcotte
Technical Files (5)
Publishing Coordination (2)